SANDIA REPORT
SAND2020-13076
Printed November 2020

Sandia National Laboratories

Assessment of AFM – KPFM and SSRM for Measuring and Characterizing Materials Aging Processes

Ana B Baca

Prepared by
Sandia National Laboratories
Albuquerque, New Mexico
87185 and Livermore,
California 94550

Issued by Sandia National Laboratories, operated for the United States Department of Energy by National Technology & Engineering Solutions of Sandia, LLC.

Available to DOE and DOE contractors from
U.S. Department of Energy
Office of Scientific and Technical Information
P.O. Box 62
Oak Ridge, TN 37831

Telephone: (865) 576-8401
Facsimile: (865) 576-5728
E-Mail: reports@osti.gov
Online ordering: http://www.osti.gov/scitech

Available to the public from
U.S. Department of Commerce
National Technical Information Service
5301 Shawnee Rd
Alexandria, VA 22312

Telephone: (800) 553-6847
Facsimile: (703) 605-6900
E-Mail: orders@ntis.gov
Online order: https://classic.ntis.gov/help/order-methods/

ABSTRACT

Atomic Force Microscopy (AFM), in conjunction with Peak Force Kelvin Probe Force Microscopy (PF-KPFM) and Peak Force Scanning Spreading Resistance Microscopy (PF-SSRM), was used to assess changes on thin metal films that underwent accelerated aging. The AFM technique provides a relatively easy, non-destructive methodology that does not require high-vacuum facilities to obtain nanometer-scale spatial resolution of surface chemistry changes. Surface morphology, roughness, contact potential difference, and spreading resistance were monitored to qualitatively identify effects of aging - morphology changes and oxidation of Au, Al, Cu thin film standards as well as diffusion of CuAu and AlAu thin film stacks at 65°C under dried nitrogen flow conditions. AFM PF-KPFM and PF-SSRM modes have been exercised, refined and have proven to be viable and necessary early aging detection tools.

ACKNOWLEDGEMENTS

I want to acknowledge the many who contributed to this project, Material Scientists at Sandia National Laboratories - Paul Vianco, Michael Brumbach, Tony Ohlhausen, Trey Pinon, David Scrymgeour for technical guidance on experimental design, results and conclusions. Rebecca Chow, Samantha Rosenberg and Dominic Casalnuovo for AES, XPS, AFM and data analysis support.

CONTENTS

1. Introduction 10
   1.1. Overview of Document 10
   1.2. Background and Significance 10
   1.3. Measurement Techniques 11
   1.4. KPFM 12
   1.5. SSRM 12
   1.6. Variables Impacting Electrical Measurements 14
      1.6.1. Tip wear 14
      1.6.2. Surface charges 14
2. Experimental Procedure 16
   2.1. Thin Metal Film Fabrication 16
   2.2. Aging Study 16
   2.3. Characterization 17
3. Results 19
   3.1. Morphology 19
      3.1.1. Au Thin Film Standard 19
      3.1.2. Al Thin Film Standard 21
      3.1.3. Cu Thin Film Standard 23
      3.1.4. Al/Au Thin Film Stack 26
      3.1.5. Cu/Au Thin Film Stack 27
      3.1.6. Roughness 29
   3.2. KPFM CPD 30
      3.2.1. Au Thin Film Standard 31
      3.2.2. Al Thin Film Standard 33
      3.2.3. Cu Thin Film Standard 35
      3.2.4. Al/Au Thin Film Stack 36
      3.2.5. Cu/Au Thin Film Stack 38
   3.3. SSRM Resistivity 40
4. Discussion 43
5. Conclusion 44

LIST OF FIGURES

Figure 1-1. Schematic of AFM and KPFM mechanics. 3
Figure 1-2. Operation of KPFM and producted signals. 4
Figure 2-1. Schematic representation of thin film stacks and anticipated results. 16
Figure 2-2. Analysis locations around FIB fiducial. 8
Figure 3-1. AFM height sensor 2μm images of all unaged and aged materials. 19
Figure 3-2. AFM 2μm height sensor Au standard.. 20
Figure 3-3. 2μm SEM and AES elemental maps of Au control sample. 20
Figure 3-4. AFM 2μm height sensor images of Al standard.. 2
Figure 3-5. 2μm SEM and AES elemental maps of Al control sample. 22
Figure 3-6. Comparison of unaged and aged 2 μm AFM heigh sensor images of Cu control sample.. 23
Figure 3-7. SEM image of large particle on aged Cu thin film and corresponding EDS image 24
Figure 3-8. 2μm AES SEM and elemental maps of unaged and aged Cu surface. 25
Figure 3-9. Granular structure became less defined over aging of Al/Au thin film stack surface. 26
Figure 3-10. 2μm SEM and elemental maps of Al/Au thin film stack unaged and aged 27
Figure 3-11. Grain structure changes in AFM height sensor 2 μm images over aging for Cu/Au thin film stack. 28
Figure 3-12. 2 μm SEM and AES elemental maps of Cu/Au thin film of unaged and aged surface 28
Figure 3-13. Roughness data for all materials. 30
Figure 3-14. 2μm height sensor images of all unaged and aged materials. 31
Figure 3-15. 2 μm KPFM and height sensor images of Au surface.. 32
Figure 3-16. 2μm SEM and AES elemental maps of Au control sample 33
Figure 3-17. 2 μm KPFM and height sensor images of Al surface. 34
Figure 3-18. 2μm SEM and AES elemental maps of Al control sample 34
Figure 3-19. 2 μm KPFM and height sensor images of Cu surface. 35
Figure 3-20. 2μm SEM and AES elemental maps of Cu control sample 36
Figure 3-21. 2 μm KPFM and height sensor images of Al/Au thin film stack surface. 37
Figure 3-22. 2μm SEM and AES elemental maps of Al/Au control sample 37
Figure 3-23. 2 μm KPFM and height sensor images of Cu/Au thin film stack surface. 38
Figure 3-24. 2μm SEM and AES elemental maps of Cu/Au control sample 39
Figure 3-25. Vdc values for unaged and aged samples 40
Figure 3-26. 20 μm topography and surface mechanical property images of Cu/Au thin film stack. 40
Figure 3-27. Resistivity data for unaged and aged surfaces. 41

LIST OF TABLES

Tabel 3-1. AES results of atomic concentrations [%] of elements found on the unaged and aged Au surface. 21
Tabel 3-2. XPS results of atomic concentrations [%] of elements found on the unaged and aged Au surface. 21
Tabel 3-3. AES results of atomic concentrations [%] of elements found on the unaged and aged Al surface. 23
Tabel 3-4. XPS results of atomic concentrations [%] of elements found on the unaged and aged Al surface. 23
Tabel 3-5. AES results of atomic concentrations [%] of elements found on the unaged and aged Cu surface. 25
Tabel 3-6. XPS results of atomic concentrations [%] of elements found on the unaged and aged Cu surface. 25
Tabel 3-7. AES results of atomic concentrations [%] of elements found on the unaged and aged Al/Au surface. 27
Tabel 3-8. XPS results of atomic concentrations [%] of elements found on the unaged and aged Al/Au surface. 7
Tabel 3-9. AES results of atomic concentrations [%] of elements found on the unaged and aged Cu/Au surface. 29
Tabel 3-10. XPS results of atomic concentrations [%] of elements found on the unaged and aged Cu/Au surface. 29

This page left blank

ACRONYMS AND DEFINITIONS

Abbreviation	Definition
AES	Auger electron spectroscopy
AFM	atomic force microscopy
Al	aluminum
Au	gold
CPD	contact potential difference
Cu	copper
FIB	focused ion beam
KPFM	Kelvin probe force microscopy
PF-AFM	peak force atomic force microscopy
Si	silicon
SKP	scanning Kelvin probe
SSRM	scanning spreading resistance microscopy
UPS	ultraviolet photoelectron spectroscopy
Vdc	voltage of direct current

1. INTRODUCTION

1.1. Overview of Document

The objective of this investigation is the evaluation and improvement of Atomic Force Microscopy (AFM), in conjunction with Peak Force Kelvin Probe Force Microscopy (PF-KPFM) and Scanning Spreading Resistance Microscopy (SSRM) modes as nanoscale aging characterization tools. These techniques will be studied in a dry, inert environment using thin metal films and thin metal film stacks conditioned at 65°C up to 200 hours in order to study morphology, surface chemistry changes on Au, Al and Cu thin films, as well as assess diffusion of Al and Cu through Au thin film stacks .

Chapter 1 describes the importance of material aging concepts for the materials of interest, compares available measurement techniques, with emphasis on the KPFM and SSRM techniques, and the variables that impact the quality and reliability of these measurements. In Chapter 2 experimental setup and analysis procedures are described. Chapter 3 details the results of all experiments. Chapter 4 contains discussion of results and Chapter 5 presents conclusions and explores future ideas in further developing AFM-KPFM and SSRM as aging characterization techniques.

1.2. Background and Significance

Over time in ambient conditions materials react with their environment resulting in changes of material properties. For instance, metals oxidize, corrode, and diffuse into one another at interfaces. This natural consequence of chemical potentials is enhanced at temperatures above 23°C. These physical and chemical changes can often alter the material properties to such an extent that they may render them unable to meet their intended function. Materials aging is a high-consequence failure mode in electronic systems [1]. Typical aging mechanisms manifest themselves as diffusion, oxidation, and corrosion [2-4]. Morphology changes, oxidation and diffusion will be the focus of this study.

Electrical contacts rely on interfacing surfaces to act as pathways for the transport of electrical current [5-7]. It is a common strategy to use multiple materials to meet performance needs. One such strategy is the plating of one metal onto another. Using Au as a plating metal optimizes nobility against oxidation, minimizes contact force, and provides high electrical conductivity at the interface [8, 9]. Using Cu as the bulk material optimizes elastic modulus, strength, cost, and is more readily available [8, 9]. Electroplating is the most commonly used process for Au plating electrical components in mass production [1, 10]. While physical vapor deposition processes such as sputtering or metal evaporation are popular environmental friendly alternatives to electroplating [11], these processes typically produce films with extremely fine grain structures, on the order of tens of nanometers [2, 3, 12], that are sometimes crystallographically textured, and with a variety of defects, which provide pathways for diffusion that will eventually lead to contact degradation [8].

Physical properties, such as surface morphology and roughness, as well as surface chemistry of metallic interconnections, and how they change in their operating environment must be understood to further the applications of nanotechnology [3]. Not only do size and shape of grain structures impact interfacing materials [2], but growth, structure and thickness of surface oxide layers alter electrical properties as well [3]. Aluminum oxide is known for its resistive properties [3] while changes in resistivity or conductivity of Cu oxide is dependent on the degree of oxidation and

thickness [12]. It is well known that physical and chemical properties of Au remain stable under most conditions but is a notorious getter for surface contamination [2, 13-15].

Solid state diffusion in Au plated contacts has been the subject of numerous studies [5, 10, 11, 16, 17]. Pinnel [10, 18] summarized the three major mechanisms in Au-Cu diffusion. The first one, which is called lattice or bulk diffusion, is a two-way process where Au diffuses into Cu while Cu into Au. The second diffusion mechanism relies on defects such as dislocations, twins, and grain boundaries and is commonly referred to as defect path or pipe diffusion. This mechanism is more prevalent in thin films synthesized by physical vapor deposition processes and electroplating as fine grain structures and columnar grain boundaries are created. While the activation energy of bulk diffusion is highly temperature dependent, the defect path or pipe diffusion is less dependent on temperature and has a lower activation energy because of available vacant sites that enable atomic movement and thereby is usually the more dominant mechanism near ambient operating conditions [10, 18]. The third mechanism results in the formation of intermetallic compounds between Cu and Au. Although the growth rate is relatively low, the intermetallics, which are typically brittle, can result in delamination of the Au films [8]. It is now common practice for a nickel layer to be placed between the Au and Cu to prevent interdiffusion [8].

Nonetheless, the Au/Cu system is of interest in this study because they readily interdiffuse at ambient conditions and challenges the detection limits of the KPFM and SSRM techniques. Diffusion phenomena in the Au/Al couple results in growth of intermetallic regions which can impact electrical conductivity via formation of voids and cracks caused by a difference in diffusion rates of metal atoms. These voids are referred to as Kirkendall voids [19, 20] and is a common phenomenon in the Au to Al wire-ball bonding process widely known throughout the semiconductor industry [9].

Such mechanisms can degrade the electrical properties of connectors, relays, wire bonds, and other interconnections [8]. Lost performance not only impacts the device in question but can also affect the function and reliability of next-level assemblies. The detection of changes to materials surfaces at the nanometer-scale resolution provides means to identify aging processes at their earliest stages before they manifest into latent failures that impact system-level performance and reliability.

1.3. Measurement Techniques

Characterizing aging materials on the nanoscale is an important primary screening capability to identify potential material failure indicators [2, 3, 12]. In this work, we focus on the use of Peak Force (PF) AFM in Frequency Modulated KPFM (FM-KPFM) and SSRM modes to characterize the Contact Potential Difference (CPD) and spreading resistance variations, while simultaneously measuring topography of the surface of thin film stacks.

KPFM and SSRM have been widely used to measure surface CPD and resistance on various materials at the nanoscale [2, 3, 12]. KPFM and SSRM enable characterization of local electrical properties at remote and complex areas such as interfaces in nanomaterials and junctions in semiconducting devices because of their high spatial resolution [21]. Two principal requirements challenge the quality of the intended measurements: reliability and high spatial resolution [14]. These nano-characterization requirements call for suitable tools and appropriate experimental protocols whose study and development form the basic core of this endeavor.

Alternative methods for measuring CPD are Scanning Kelvin Probe (SKP) and UV-Photoelectron Spectroscopy (UPS) [22]. SKP provides CPD information on the macro scale without topographical or spatially resolved information. UPS is done under high vacuum and does not provide spatially

resolved information. Furthermore, resistance can be measured using the 4-probe technique, however the 4-probe technique does not provide topographical or spatially resolved information.

Thus, we use PF-KPFM and SSRM to perform high spatial resolution mapping of electronic properties alongside simultaneous mapping of surface topography/roughness. In this study we investigate whether these AFM modes in conjunction with AES and XPS could be used to characterize aging in materials and serve as an additional tool to identify material degradation when it is not readily evident in "bulk" measurement techniques.

1.4. KPFM

KPFM, as a proof of principle, was first reported by Nonnenmacher and coworkers in 1991 [15]. Numerous developments to the method have been made to improve resolution and sensitivity [22-29]. Many studies have identified extraneous factors affecting the measured surface potential and found mitigating techniques [22-24, 26, 27, 29-31]. Now, it is common to obtain spatial resolution on the nanometer scale, with a resolution on the order of a few mV [16-19]. In the most simplistic form, KPFM operates on the principle of measuring the CPD between two parallel plate capacitors with a small spacing on the order of 80nm and oscillated at a periodic vibration of the plates at a certain frequency ω. By applying an external voltage to nullify the electric field between the two capacitors, the force exerted by the external field can be measured, and this force is equal to the CPD [15]. In this method, the two parallel plate capacitors are the sample and the probe tip. The relationship is described below:

$$V\_CPD=(\phi\_tip-\phi\_sample)/(-e) \qquad (1\text{-}1)$$

where Vcpd is the nulling voltage equal to the CPD, Φtip and Φsample are the work functions of tip and sample, respectively, and e is the electrical charge [20]. Thus, if the work function of the tip is known, the work function of the sample can be calculated. Figure 1-1 provides a first look at this setup. The bottom section of the schematic (labeled AFM) shows the tracking of the tip height information by the laser focused on the backside of the cantilever and reflected into a photodiode. Piezoelectric tubes control the cantilevers X, Y and Z positions. The upper section of the schematic (labeled FM-KPFM) demonstrates the mechanisms responsible for producing the FM-KPFM measurement.

1.5. SSRM

Scanning Spreading Resistance Microscopy - SSRM has been developed out of the need to measure 2D carrier profiling on devices in the semiconductor industry [32]. SSRM measures a sample's local spreading resistance between the sample and tip by applying a DC bias and using a logarithmic amplifier, while simultaneously characterizing topography by the peak force tapping method. Spatial resolution is dependent on probe radius and shape. Resistivity values depend on surface chemistry, concentrations, energy distributions and force between probe and sample. A high tip-sample force is often necessary to achieve consistent, reliable resistivity values. This underscores the importance of using a diamond coated probe which has been found to be a favorable wear resistance probe [32]. Studies show that the sensitivity of the measurement drops drastically with increasing surface oxide thicknesses. A larger tip-to-sample force can aid in this situation but is not always successful [32]. Thus the spreading resistance image contrast obtained in this manner reflects variations in material conductance/resistance properties on the surface, with lower spreading resistance corresponding to higher conductivity [32].

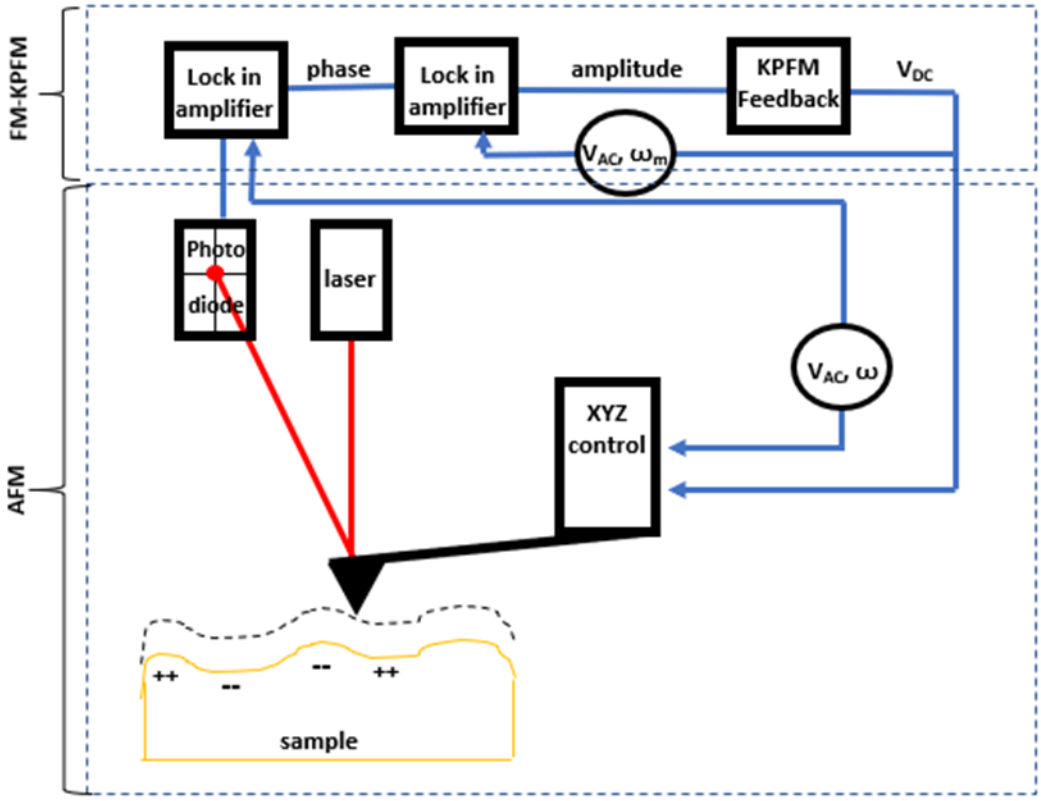

Figure 1-1. Schematic of AFM and KPFM mechanics.

To accurately measure the CPD between the surface and the tip, the cantilever is mechanically driven with an AC bias at frequency ω. The cantilever oscillation phase is measured by a lock-in amplifier. This phase signal is sent to a second lock-in amplifier to obtain the AC signal's amplitude of the 2nd harmonic frequency ωm. A feedback loop is employed to minimize this AC signal amplitude until it directly offsets the induced electric field gradient, as shown schematically in Figure 1-1.

In addition, it is common practice to operate KPFM in an interleave mode in which the AFM will measure and record the topography for a line scan in the first pass, lift to a user-defined height – 80nm in this case, and measure the CPD on the second pass, using the topographical information to keep the lift height constant. This method is one of the main techniques to prevent topography correlated artifacts in the measurement [29] and is illustrated in Figure 1-2. The left side of Figure 1-2 shows the steps the cantilever cycles through to perform the KPFM measurement. The bottom right schematic demonstrates a topographical profile and the top right image demonstrates the CPD profile (interleave scan). Step 1 is the topographical pass, step 2 is the lift, and step 3 is the CPD measurement pass giving the output signal depicted at the top right.

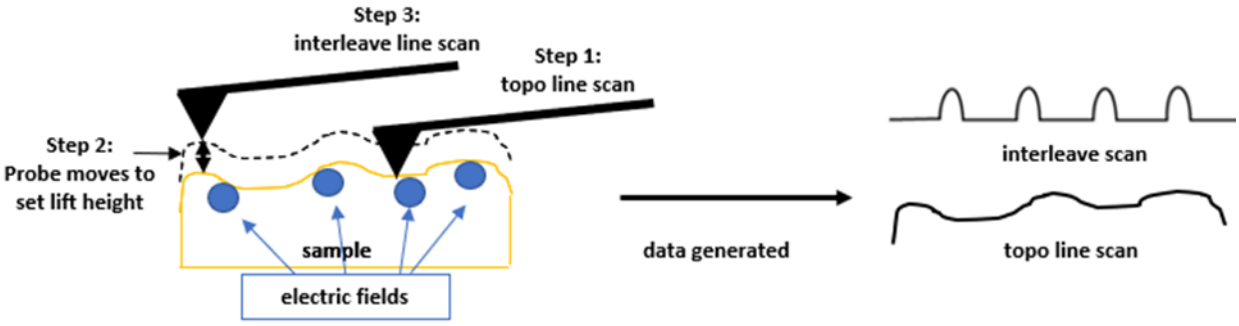

Figure 1-2. Depiction of expected signals when KPFM probes electric fields embedded in a surface.

Two common modes of measuring KPFM are amplitude modulated (AM) and frequency modulated (FM). In AM mode, the KPFM measures the force at ω, directly from the perturbation in amplitude of the cantilever oscillation, whereas in FM mode, the force is detected by the frequency shift at ω, and this shift is nullified by an applied voltage [26]. The difference between the two techniques offer distinct advantages - FM-KPFM measures a higher spatial resolution since the gradient in the electrostatic force is what is detected, rather than the force itself. AM-KPFM measurements yield higher signal to noise ratio than FM [21]; however, the surface potential measurement using AM is significantly affected by the stray capacitance between the cantilever and surface, which introduces artifacts in KPFM images [31].

It should be noted that KPFM measures relative differences, not absolute values. Thus, in order to determine sample work function, the tip work function must be known and invariable, which is not always the case. Wearing of the tip as well as sample surface conditions change the tip composition, size and shape which can distort the measured CPD values [22]. These variables will be discussed in the following section.

1.6. Variables Impacting Electrical Measurements

1.6.1. Tip wear

Peak Force Tapping AFM was employed as the topographical characterization method in this study. Peak Force Tapping is a measurement technique whereby the probe tip periodically taps the sample at a set force as the probe rasters across the sample. The force is measured directly by the deflection of the cantilever. A feedback loop controls the force. Since the tip physically interacts with the sample there is the possibility that the tip coating could wear over the course of the image acquisition. Furthermore, contamination of the tip is a possibility, which could significantly degrade the CPD measurement. To ensure CPD measurement reproducibility, a tip health protocol developed by Kaja [23] was employed in which the Vdc was measured at specific predetermined locations to determine consistent measured values.

1.6.2. Surface charges

Variations in CPD may be due to surface conditions including uneven distribution of adsorbates, crystallographic orientation or variation in surface local geometry. These variables are known as

Patch Charge [22]. Many surface phenomena impact surface characterization, especially electrical characterization. Two major contributors are surface dipole layers and adsorbates, including humidity [2, 3, 22, 32]. The surface dipole layer can form by a charge distribution forming and then the opposite charge distribution being created to balance overall surface charge. A dipole layer induces an energy step that must be overcome for electrons to escape the surface [22]. This is an intrinsic phenomenon that occurs in conducting materials and may vary substantially depending on composition, environmental and surface conditions. Adsorbates can create surface dipoles which form from the transfer of charge between the adsorbate and the substrate. The composition and quantity of the adsorbate may induce a large degree of variability in the CPD measurement [22].

2. EXPERIMENTAL PROCEDURE

2.1. Thin Metal Film Fabrication

Polished single crystal silicon (Si)wafer substrates were cleaned with a Lenium degrease, then acetone followed by 20 minutes exposure of UV/O3. Thin metal films were evaporated on the silicon substrates. Five thin film samples were made, beginning with the deposition of a 5 nm chromium (Cr) adhesion layer on the Si surface. Sample 1 was made with 500 nm gold (Au) put down on top of the adhesion layer. Sample 2 was made with 500 nm aluminum (Al) deposited on top of the adhesion layer. Sample 3 was made with 500 nm copper (Cu) put down on top of the adhesion layer. Sample 4 was made with 500 nm Al put down on top of the adhesion layer followed by 500 nm thick Au top layer. Sample 5 was made with 500 nm Cu put down on top of the adhesion layer followed by 500 nm thick Au top layer. The characterization analysis will be performed on the top layer of all samples. Samples 1-3 (Au, Al, Cu) are for control purposes. Samples 4 (Al/Au thin film stack) and 5 (Cu/Au thin film stack) are expected to show constituent changes on the Au surface layer as either Cu or Al diffuse through defects in the Au layer to the latter's surface. The objective of the analysis is to detect Cu or Al islands forming on the surface of the Au indicating locations of Au grain boundaries. Figure 2-1 is a schematic of the thin metal film cross sections where we see Cu or Al particles diffusing from the underlaying layer up through Au grain boundaries and forming islands on the surface of the Au layer.

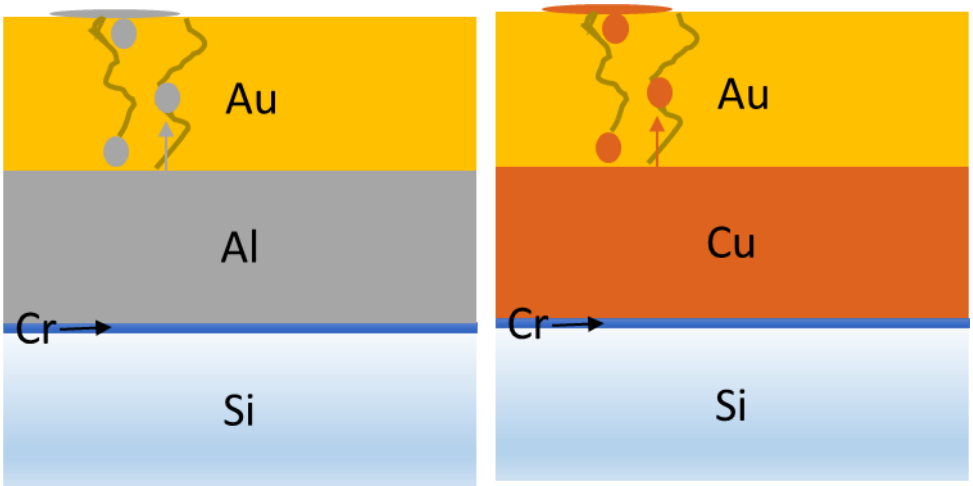

Figure 2-1. Evaporated deposition samples. Si followed by 5nm Cr adhesion layer, 500nm Al (left) or Cu (right) and 500 nm Au. Cu and Al atoms migrating up through Au grain boundaries and forming islands on the surface of the Au.

2.2. Aging Study

Typical operating temperatures for electrical connectors in industrial applications range between 80°C and 135°C [8]. In the current study, accelerated aging experiments on thin metal film specimens were conducted at temperatures of 65°C in an attempt to capture the very beginning indications of grain boundary diffusion when Cu or Al atoms first appear at the Au surface, but before completely covering it. Initial studies included samples with varying Au thicknesses (0.5 to 5 μm) over Cu. These experiments were carried out under ambient conditions at a variety of

temperatures (50,100 and 125°C) in ovens and analyzed following 8 hours, 24 hours, 96 hours (4 days), and 216 hours (9 days) of aging to encourage grain boundary diffusion. The rationale to select a variety of temperature and time conditions was to probe overall changes in order to select conditions that would optimize the study of grain boundary diffusion [33].

Oxidation was visibly evident on the 100 and 125°C samples. In attempt to avoid topographical complications associated with oxidation effects, the subsequent experiments were conducted by aging under dry nitrogen on a heating stage in the AFM environmental enclosure and analyzed at the same time intervals 8 hours, 24 hours, 96 hours (4 days), and 216 hours (9 days). To minimize variables associated with varying thicknesses of layers, which was discovered in initial studies, a 0.5 μm Au thickness was chosen for the study presented in this report

In a previously attempted experiment, a FIB cross section of one of these samples was investigated, but analysis was not possible because the area of interest was difficult to access with the AFM probe and the surface was not uniform enough for successful imaging.

2.3. Characterization

Atomic Force Microscopy measurements were performed using Peak Force KPFM and Peak Force SSRM modes on a Bruker Dimension Icon Atomic Force Microscope equipped with an environmental chamber style tip holder on an in-situ heater stage. Every analysis was performed under dry nitrogen environment using a closed loop scan head, which has a maximum horizontal scanning range of $90 \times 90\ \mu m^2$ and a vertical scanning range up to 8 μm. The acquisition parameters differed from the default Scanasyst (Bruker AFM software package) parameters with a 2 μm analysis area, a scan rate of 0.5 Hz, samples/line of 512, Peak Force Setpoint of 20 nN and the heater stage set to 65 °C between 23 °C acquired images. A topographical Height Sensor image was acquired on an area for the unaged condition once the sample was dried overnight and once again on the same area after the sample had been aged for 216 hours.

Data was processed using NanoScope software [34]. A plane fit correction was applied to all height sensor images to account for surface tilt. Rq (root mean square), 2D roughness analysis was applied to height sensor images (excluding extraneous localized regions) to characterize average roughness and changes in roughness in areas of interest before and after aging. Changes in topography such as grain sizes and structures were assessed before and after aging as well.

The Scanning Capacitance Microscopy-Platinum Iridium coated (SCM-PIT) AFM probe by Bruker was selected for use for KPFM Analysis. It is a Pt-Ir coated and Sb doped Si probe/cantilever, with the thickness of 2.5 – 3.5 μm, length of 200-250 μm, operating frequency of 60-100 kHz, and spring constant of 1-5 N/m. The probe has a tip height of 10-15 μm and radius ~20 nm. A DDESP-FM-V2 probe by Bruker was used for SSRM analysis. It is a conductive diamond coated and Sb doped Si probe/cantilever, with the thickness of 2.2 – 3.7 μm, length of 225-235 μm, frequency of 80-130 kHz, and spring constant of 3-12 N/m. The probe has a tip height of 10-15 μm and radius ~100 nm. All samples were mounted on stainless steel AFM pucks and electrically grounded to the puck using silver paint. The optimized KPFM acquisition parameters differed from the default parameters with an interleave lift height of 80 nm and a driving amplitude of 6000 mV. A KPFM image was acquired simultaneously with the height sensor image. Two different KPFM measurements were done for this study – Vdc measurements and 2D imaging. The Vdc measurements were taken to

determine CPD at 8 separate point locations relative to a FIB fiducial, shown in Figure 2-2. This served to eliminate topography as a variable from the CPD value as these measurements were done at a scan size of 0 nm - a single point.

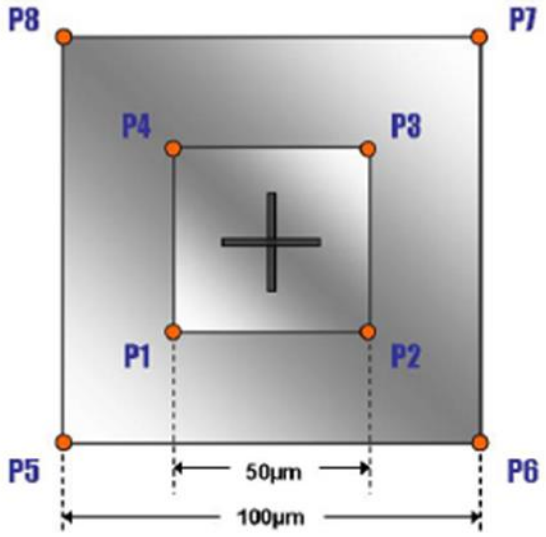

Figure 2-2. 8 locations around FIB fiducial where point KPFM measurements were made

The both KPFM image and Vdc point measurements locations were chosen at random but consistent for each sample in order to correlate exact analysis location with AES. Data was processed using NanoScope software. A first order flattening correction was applied to KPFM 2D images and Vdc measurements to account for slow axis variability such as electronic drift and particulate artifacts. A 2D Rq roughness analysis calculation was applied to the 2D and Vdc data to characterize average CPD values. By calculating the "roughness" of the data using the NanoScope software analysis package, an average value for each image is determined as well as variability of the measurement.

AES was performed with a Physical Electronics 690 Auger spectrometer operated at pressures < 2×10^{-9} Torr. The instrument utilizes a double-pass cylindrical mirror analyzer. Images and spectra were obtained using a field-emission tip with beam energy of 10 kV at 10nA. Data was processed using the Physical Electronics Multi-Pack software.

X-ray Photoelectron Spectroscopy (XPS) was performed with a Kratos AXIS Supra instrument. X-ray excitation was from a monochromatic Al Kα (1486.7 eV) source. Individual spots analyzed were an elliptical area of 300 x 700 µm. Survey spectra were recorded at either 80 eV or 160 eV pass energy. High resolution spectra were taken at 20 eV pass energy. Base pressures were less than 5×10^{-9} Torr.

3. RESULTS

Evidence of morphology changes, oxidation, and diffusion have been identified by all techniques – AFM, KPFM, SSRM and confirmed with AES and XPS which will be presented in the following sections. Each aged standard – Au, Al and Cu along with AlAu thin film stack and CuAu thin film stack will be discussed and compared with the unaged condition in each section – morphology and roughness, KPFM and SSRM.

3.1. Morphology

Morphology changes were observed as changes in grain shapes, sizes and shifting as well as particulate formation. Roughness analysis was also conducted over the course of exposure for samples. To serve as a visual aid, an overview of height sensor images of each sample is shown in Figure 3-1, in the unaged condition (top row) and aged condition (bottom row).

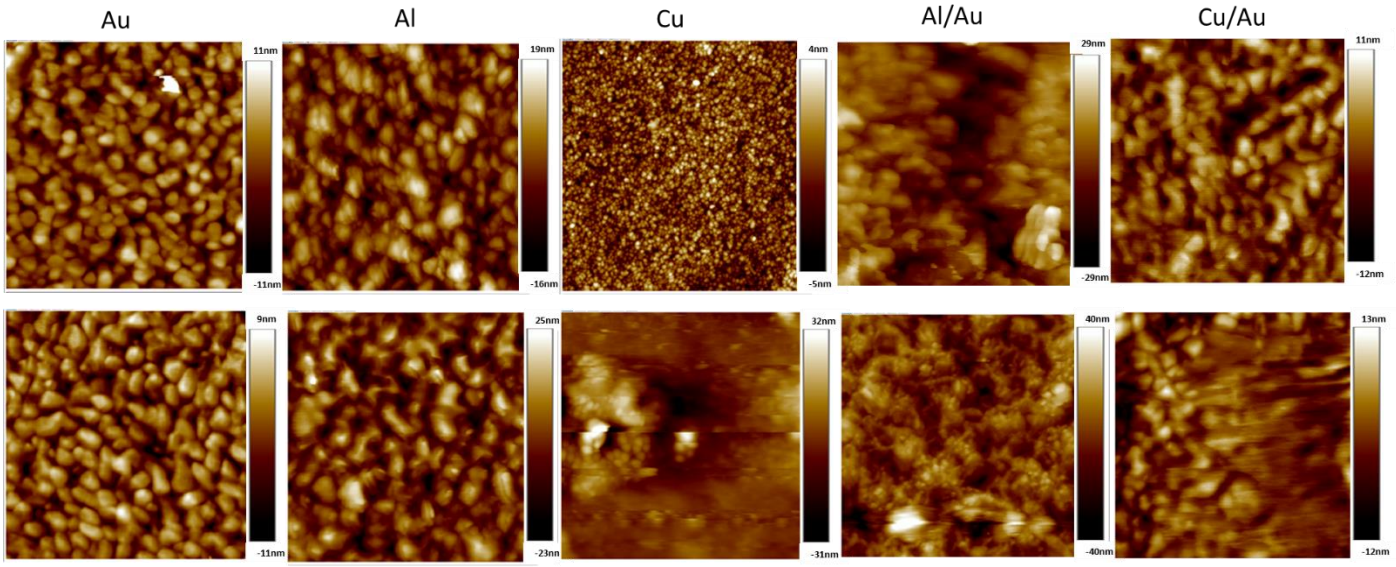

Figure 3-1. AFM height sensor 2µm images of all unaged (top row) and aged (bottom row) materials.

3.1.1. Au Thin Film Standard

Slight morphological change is observed for the Au standard surface as shown in height sensor images in Figure 3-2 where a) unaged surface is compared with b) the aged Au surface where grains appear shifted and slightly enlarged. Figure 3-3 shows SEM images (a and e) and elemental maps (b-g) for the unaged Au (top row) and aged Au (bottom row) surface. Elemental maps (c and g) show C on the surface of Au (b and f) images.

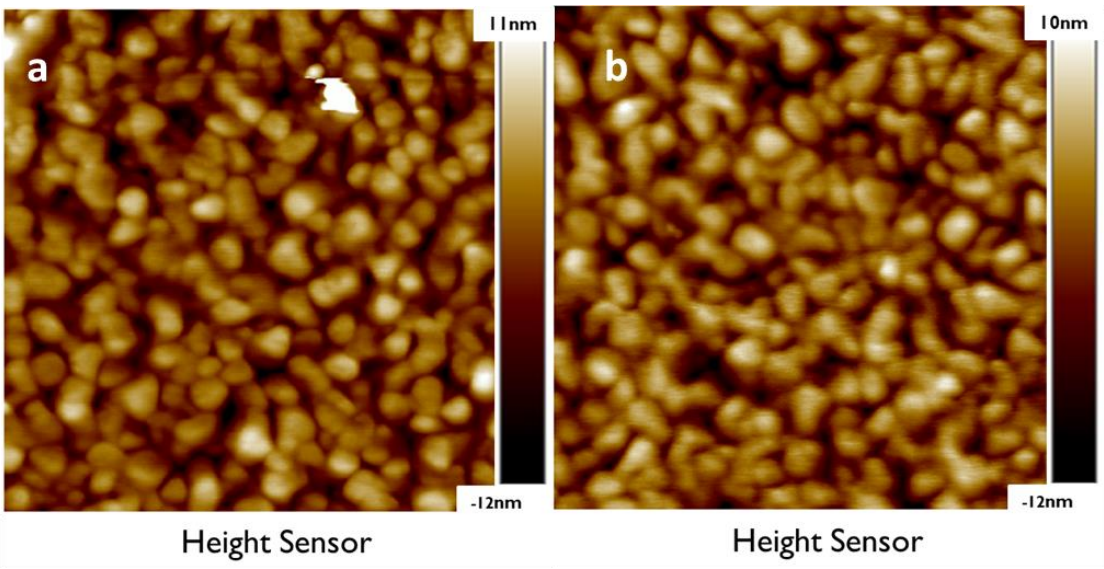

Figure 3-2. AFM height sensor 2µm images of (a) unaged Au surface and (b) aged Au surface

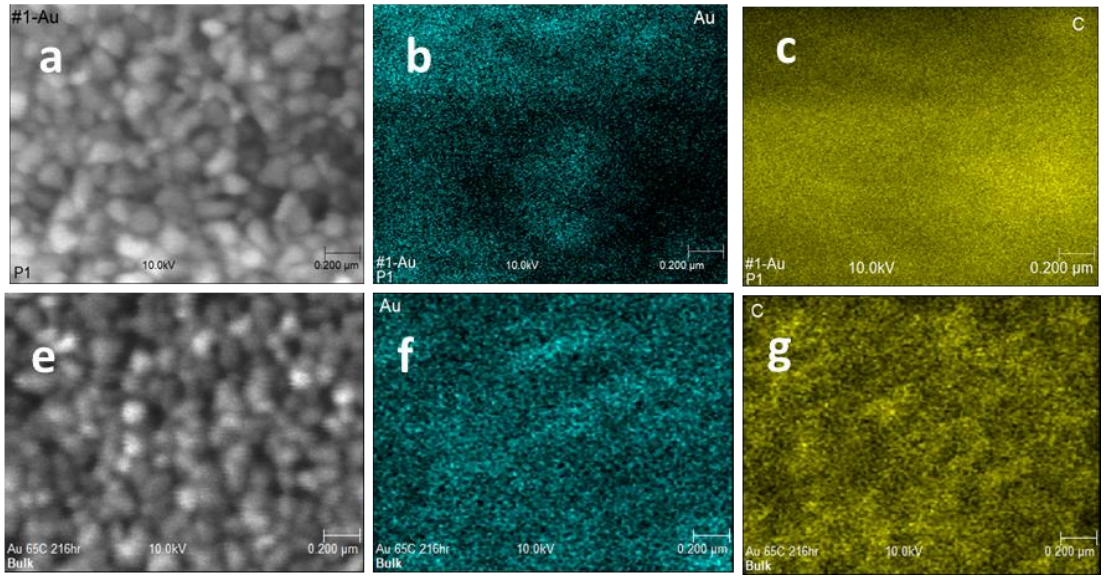

Figure 3-3. 2µm SEM (a and e) AES elemental maps (b-g) images of unaged (top row) and aged (bottom row) of Au surface. Elemental map C images (c and g) and Au images (b and f)

Results of AES analysis in Table 3-1 summarize the concentration of elements on the unaged and aged Au surface. C concentration increased on aged surface. This masks the Au, decreasing the percentage of Au detected on the aged surface. A small amount of N was detected on aged sample as well.

Table 3-1. AES atomic concentrations of elements found on the unaged (top row) and aged (bottom row) of the Au surface.

Atomic Concentration (%)			
Au standard	Au	C	N
Unaged	73.9	26.1	---
Aged	38.9	58.1	3.0

Results of XPS analysis in Table 3-2 shows atomic concentration of elements on the surfaces of the unaged and aged Au surface. C concentration increased over the course of aging as well as O. The increase in O and C is likely from atmospheric exposure. S was detected on the unaged surface which is likely a trace contaminant.

Table 3-2. XPS atomic concentrations of elements found on the unaged (top row) and aged (bottom row) of the Au surface.

Au standard	Au 4d %	C 1s %	O 1s %	S 2p %
Unaged	70.1	26.6	3.2	0.4
Aged	52.7	38.8	8.0	---

3.1.2. Al Thin Film Standard

The Al surface showed little morphological change as shown in height sensor images in Figure 3-4 (a) unaged with aged Al surface (b). Figure 3-5 shows SEM images (a and e) and AES elemental maps (b-h) of the unaged Al (top row) and aged Al (bottom row) surface. Elemental maps (b and f) are O, elemental maps (c and g) show Al and maps (d and h) show C concentration on the Al surface.

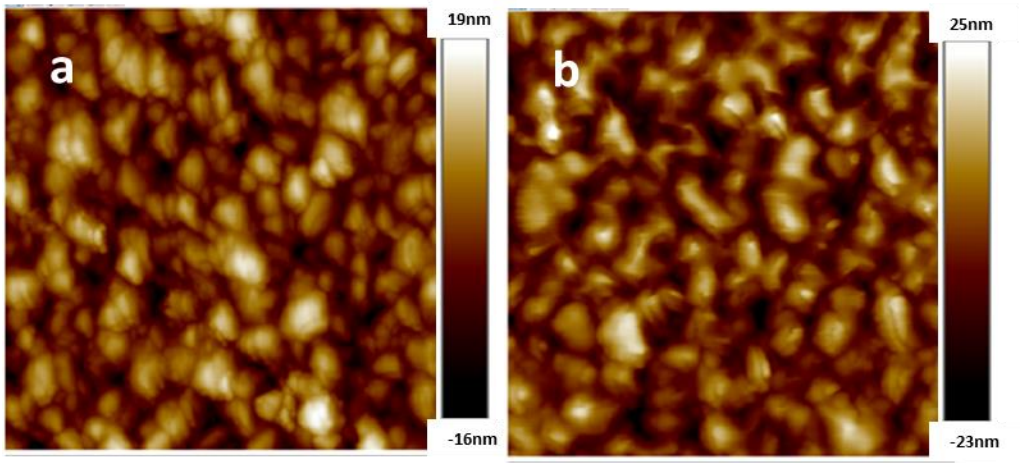

Figure 3-4. AFM height sensor 2µm images of unaged (a) and aged Al surface (b)

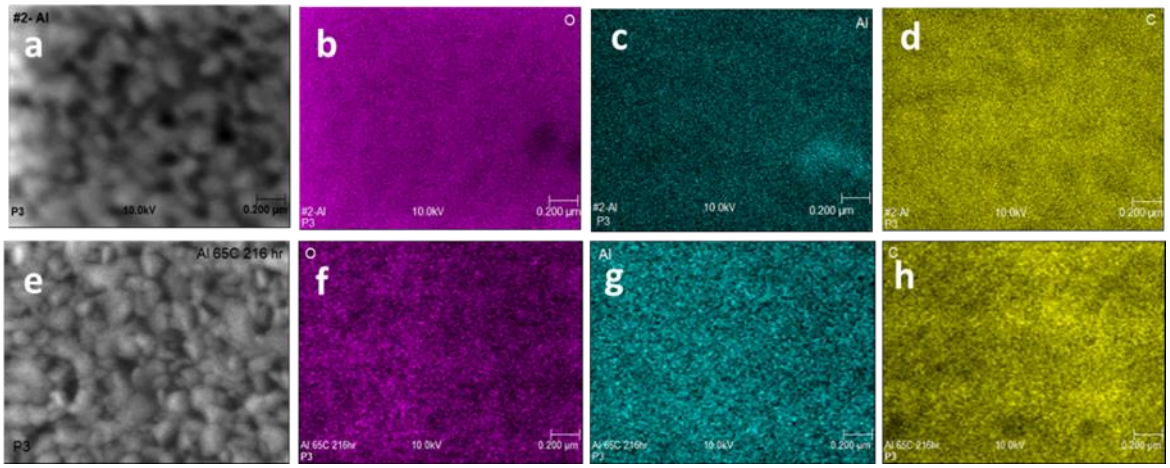

Figure 3-5. 2µm SEM (a and e) AES elemental maps (b-g) of unaged (top row) and aged (bottom row) Al surface. O maps (b and f), Al maps (c and g) and C maps (d and h)

The AES analysis summarized in Table 3-3 shows atomic concentration of elements on the surface of the unaged and aged Al surface. C concentration increased over the course of aging as well as the O which is due to oxidation which also decreases the Al concentration. Si was detected on aged sample as well.

Table 3-3. AES atomic concentrations of elements found on the unaged (top row) and aged (bottom row) of the Al surface.

Atomic Concentration (%)				
Al standard	C	Al	O	Si
Unaged	34.9	34.0	30.9	---
Aged	44.7	27.6	26.1	1.6

XPS analysis summarized in Table 3-4 shows atomic concentration of elements on the surface of the unaged and aged Al surface. C concentration increased over the course of aging as well as the O which is likely due to contamination and oxidation. Mg and Si was detected on the unaged surface and N was detected on the aged surface. These are likely due to atmospheric contamination.

Table 3-4. XPS atomic concentrations of elements found on the unaged (top row) and aged (bottom row) of the Al surface.

Al standard	Al 2p %	C 1s %	O 1s %	Mg 2s %	Si 2p %	N 1s %
Unaged	38.5	19.5	28.9	9.7	2.6	---
Aged	35.1	31.3	33.3	---	---	0.1

3.1.3. Cu Thin Film Standard

Some notable morphological observations include large agglomerates that formed on the Cu thin film shown in Figure 3-6 where the image a) is a height sensor image of the unaged Cu thin film standard and image b) is the same surface aged. Imaging became difficult on this sample as aging time increased. Oxidation induced particulate formation and growth are most likely the source of this issue.

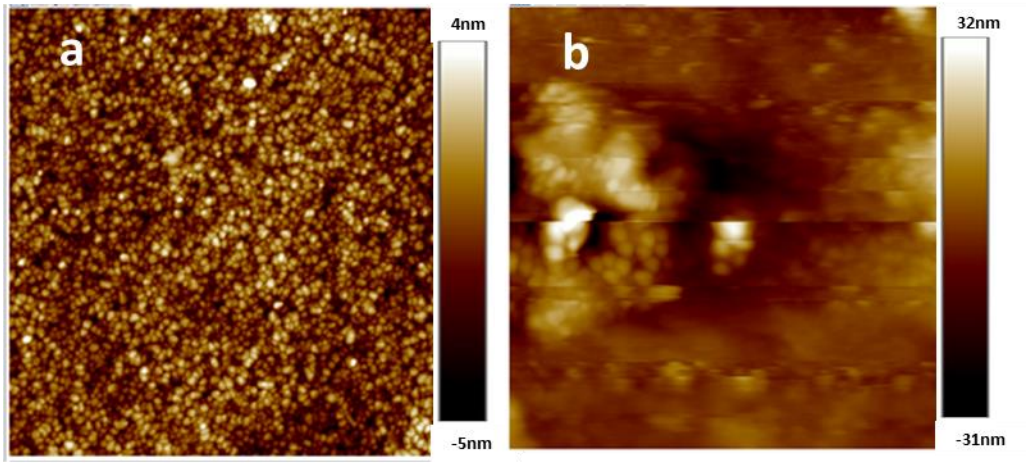

Figure 3-6. Formation of large agglomerates in aged Cu thin film (b) in AFM Height sensor 2µm images compared to unaged Cu (a)

SEM/EDS analysis Figure 3-7 (top) is a particle on the Cu surface comprised of the following elements – C, O, Al, Cu, Si and Fe. It is unclear where the Al and Fe contaminants came from, but the C is likely due to atmospheric contamination. Oxidation is likely the source of the oxygen as it covers the surface as well as the particle. It appears the Si and Fe are trace contaminants.

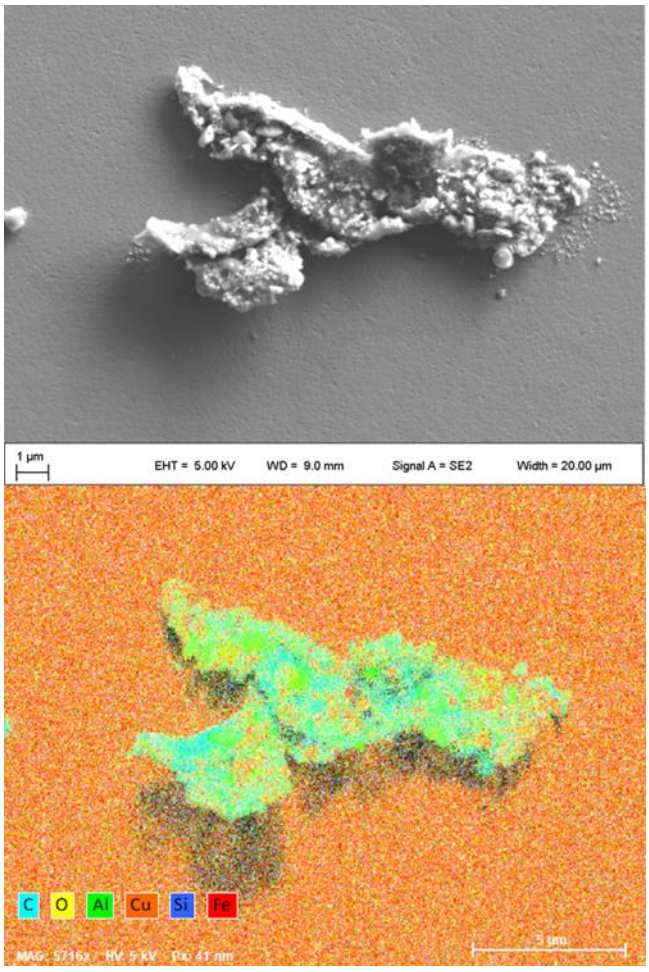

Figure 3-7. SEM image (top) of large particle on aged Cu thin film and corresponding EDS image (bottom)

Results from AES elemental mapping analysis shows oxidation and the presence of C on the unaged surface as shown in Figure 3-8, where the unaged Cu surface is the top row of images and the bottom row of images is the aged Cu surface. Images c and g are the O maps and image d is the C elemental maps. The aged surface maps confirm particulate formation. Some of the particulates are the same composition as the rest of the surface, others show the presence of Si (Figure 3-8, i).

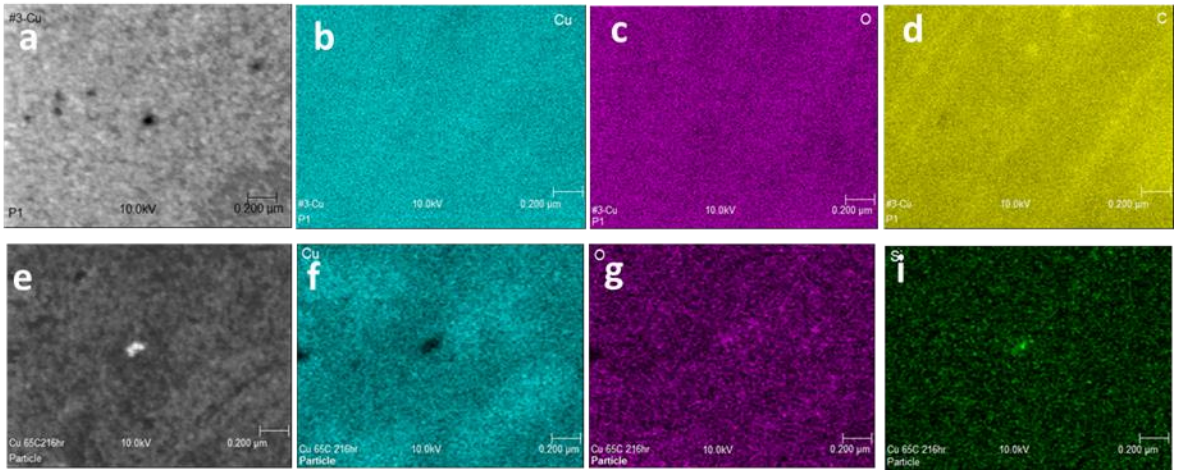

Figure 3-8. 2µm AES SEM and elemental maps of unaged Cu surface (top) and aged (bottom)

AES atomic concentrations summarized in Table 3-5 for the aged and unaged Cu surface as well as various particles found on the aged surface and their compositions. The Si, Cl, P, S, Ag and Sn contaminants likely came from the atmosphere and possibly handling.

Table 3-5. AES elemental identification on Cu unaged, aged surface and particles found on aged surface

Atomic Concentration (%)									
Cu standard	**C**	**O**	**Cu**	**Si**	**Cl**	**P**	**S**	**Ag**	**Sn**
Unaged	45.4	17.6	37.0	---	---	---	---	---	---
Aged	54.4	18.9	26.3	---	0.4	---	---	---	---
Si Particle	55.4	13.7	18.1	12.8	---	---	---	---	---
Particle	55.0	16.2	28.1	---	0.6	---	---	---	---
Large Debris	48.9	22.4	11.2	---	0.2	1.6	2.0	1.2	12.5

XPS analysis results for the Cu thin film summarized in Table 3-6 where the top row is the unaged surface and the bottom row is the aged surface element composition identifies the following elements – C, O, Cu as well as traces of F, N, S, Ag and Cl. It is unclear where the F, N, S, Ag and Cl contaminants came from, but the C is likely due to atmospheric contamination. Oxidation is likely the source of the oxygen which is surprisingly abundant on the unaged surface as well as the aged.

Table 3-6. XPS quantitative elemental identification on Cu unaged (top row) and aged (bottom row) surfaces

Cu standard	**C 1s %**	**Cu 2p %**	**F 1s %**	**N 1s %**	**O 1s %**	**S 2p %**	**Ag 3d %**	**Cl 2p %**
Unaged	48.0	18.3	0.3	0.3	33.2	---	---	---
Aged	69.1	6.2	0.0	0.1	22.3	0.2	0.3	1.0

3.1.4. Al/Au Thin Film Stack

The microstructure on the surface of the Al/Au thin film stack became less defined over the course of aging as shown in Figure 3-9 where unaged surface is on the left and the aged on the right. The unaged microstructure should have been similar to Au since it is the surface layer, but grain structure is highly dependent on underlaying structures (which would have been Al) and thickness [2, 3]. Evidence of surface oxidation was found in both AES and XPS analysis which could be the source of microstructure change. Imaging became difficult on this sample likely due to oxide formation and growth on the surface.

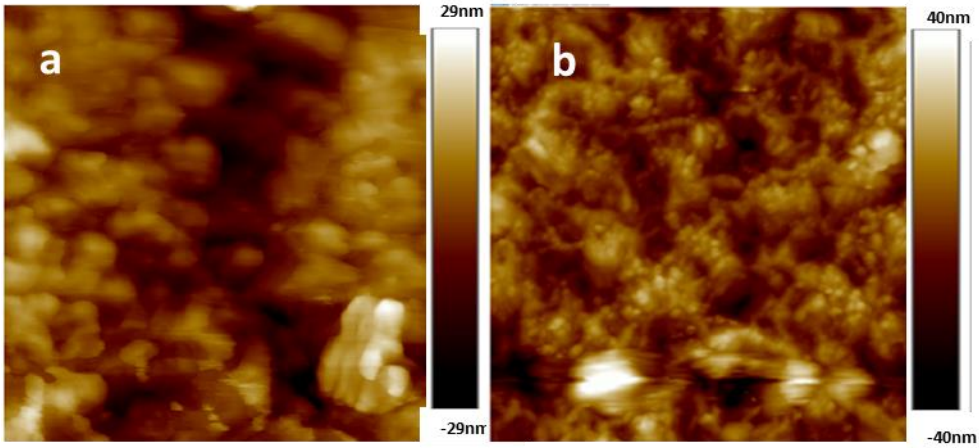

Figure 3-9. Microstructure became less defined on aged Al/Au thin film stack surface (b) in AFM height sensor 2μm images compared to unaged image (a)

Auger Electron Spectroscopy analysis detects evidence of oxidation, the presence of C and O on the unaged sample and surprisingly the presence of Al on the unaged surface as shown in Figure 3-10 where the unaged Al/Au surface is the top row of images and the bottom row of images is the aged. SEM Images are a and f, O elemental maps are images b and g, Au elemental maps are images c and h, images d and i are Al elemental maps and e and j are C maps. Al elemental map of the aged surface shows a uniform distribution of Al which indicates a bulk diffusion opposed to a grain boundary diffusion mechanism. The dark areas in images g, h and i are likely due to the C surface contamination masking specific element.

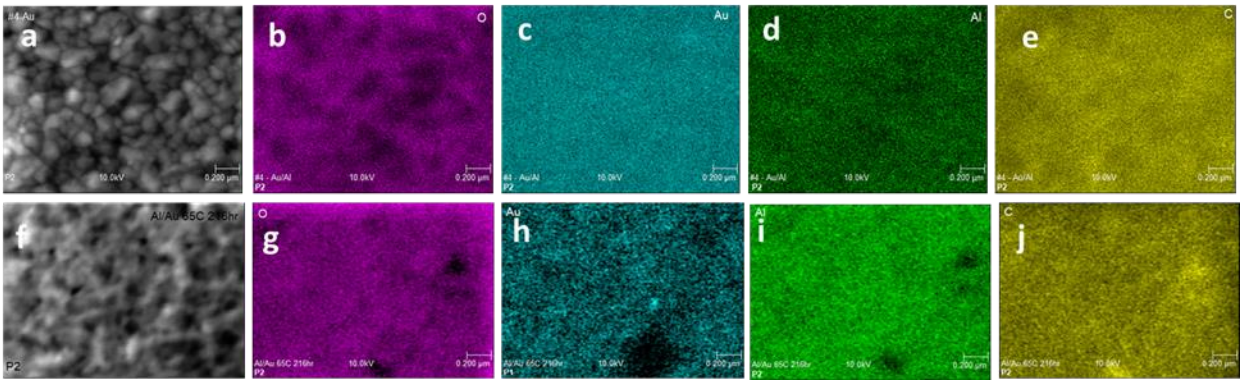

Figure 3-10. AES - 2µm SEM and elemental maps of Al/Au thin film stack unaged (top) and aged (bottom).

AES atomic concentration summarized in Table 3-7 shows an increase in O and C likely due to oxidation and contamination, respectively, and an increase in Al after aging as expected via diffusion. A small amount of Si is also presence, but the source is unknown.

Table 3-7. AES elemental identification on the surface of Al/Au unaged and aged sample.

Atomic Concentration (%)					
AlAu	C	O	Al	Au	Si
Unaged	43.5	5.6	5.7	45.3	---
Aged	46.6	18.0	22.2	7.7	5.6

XPS atomic concentration detects the presence of Al only after aging, an increase in O likely due to oxide growth, an increase in C and a decrease in Au after aging as expected via diffusion. Small amounts of F and N were also detected on the aged surface though the source is unknown as summarized in Table 3-8.

Table 3-8. XPS quantitative elemental identification on the surface of Al/Au unaged (top row) and aged (bottom row) sample.

Al/Au Stack	Al 2p %	Au 4d %	C 1s %	O 1s %	F 1s %	N 1s %
Unaged	0.0	52.2	32.5	15.3	---	---
Aged	22.3	2.4	40.2	34.2	0.2	0.8

3.1.5. Cu/Au Thin Film Stack

Microstructure became less defined and grain structures disappeared altogether over localized areas on the surface of the CuAu thin film stack as shown in Figure 3-11 (unaged on the left and aged on the right).

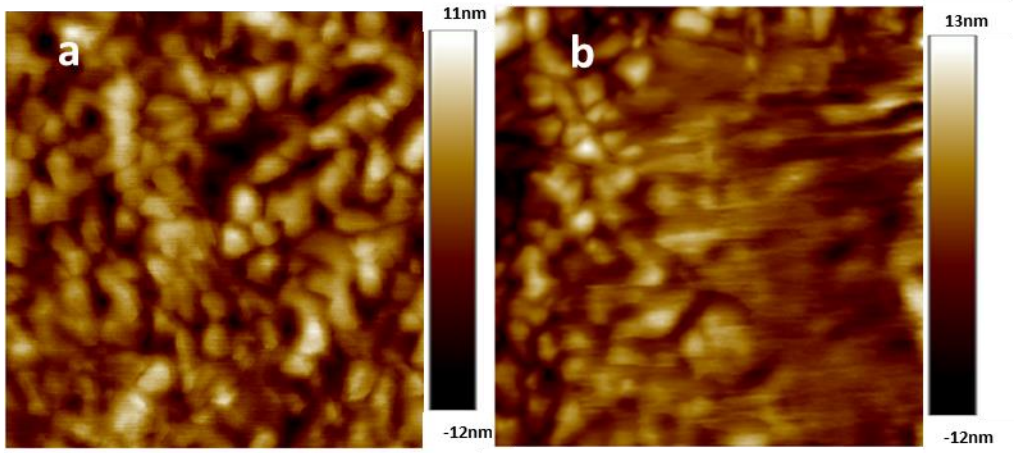

Figure 3-11. Grain structure changes in AFM height sensor 2 µm images for unaged (a) and aged (b) of Cu/Au thin film stack

Auger Electron Spectroscopy and elemental mapping analysis detects evidence of oxidation, the presence of C and O on the unaged sample and surprisingly the presence of Cu on the unaged surface as shown in Figure 3-12 where the unaged CuAu surface is the top row of images and the bottom row of images are the aged. SEM images are a and f, Cu elemental maps are b and g, Au elemental maps are c and h, re O elemental maps are d and I and C maps are e and j. Cu elemental maps of the aged surface shows a uniform distribution which indicates bulk diffusion opposed to the grain boundary diffusion mechanism. Unfortunately, there is no chemical distinction associated with the microstructure changes.

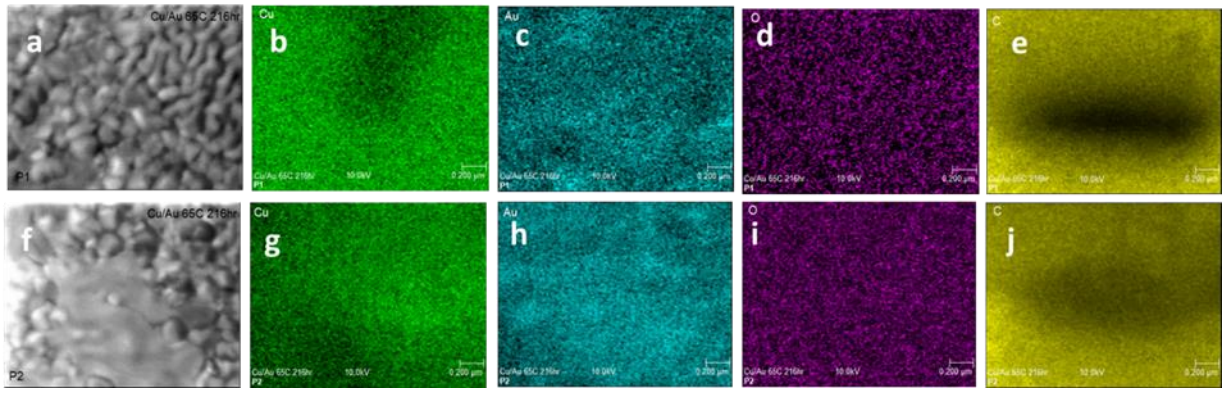

Figure 3-12. AES – 2 µm SEM and elemental maps of Cu/Au thin film of unaged (top) and aged (bottom) surface

AES atomic concentration for the Cu/Au surface shown in Table 3-9 indicates an increase in C due to atmosphere contamination, a decrease in Au and an increase in Cu after aging as expected via diffusion.

Table 3-9. AES Cu/Au thin film stack unaged (top) and aged (bottom) shows elemental concentration

Atomic Concentration (%)				
CuAu	C	Cu	Au	O
Unaged	42.8	1.1	56.1	
Aged	59.6	3.1	37.4	

XPS atomic concentration detects the presence of Cu on the unaged sample as well as the aged, an increase in O likely due to oxidation, an increase in C and a decrease in Au.

Table 3-10. XPS quantitative elemental identification on the surface of Cu/Au unaged (top row) and aged (bottom row)

Cu/Au Stack	Au 4d %	C 1s %	Cu 2p %	O 1s %
Unaged	79.8	17.7	1.5	1.0
Aged	42.3	43.1	5.0	9.5

3.1.6. Roughness

Roughness was assessed on unaged and aged surfaces during exposure to 65°C for up to 250 hours. A statistically significant change in roughness was not found. Morphology and roughness of thin films for Au, Al and Cu vary depending on deposition process and conditioning steps such as annealing and film thickness [3, 13, 15]. Grain coarsening is expected as materials are exposed to heat [2, 3, 15], however no literature was found for these materials at the temperature of 65°C for comparative purposes. Figure 3-13 shows the roughness data (Rq) over 200+ hours at 65 °C for all samples.

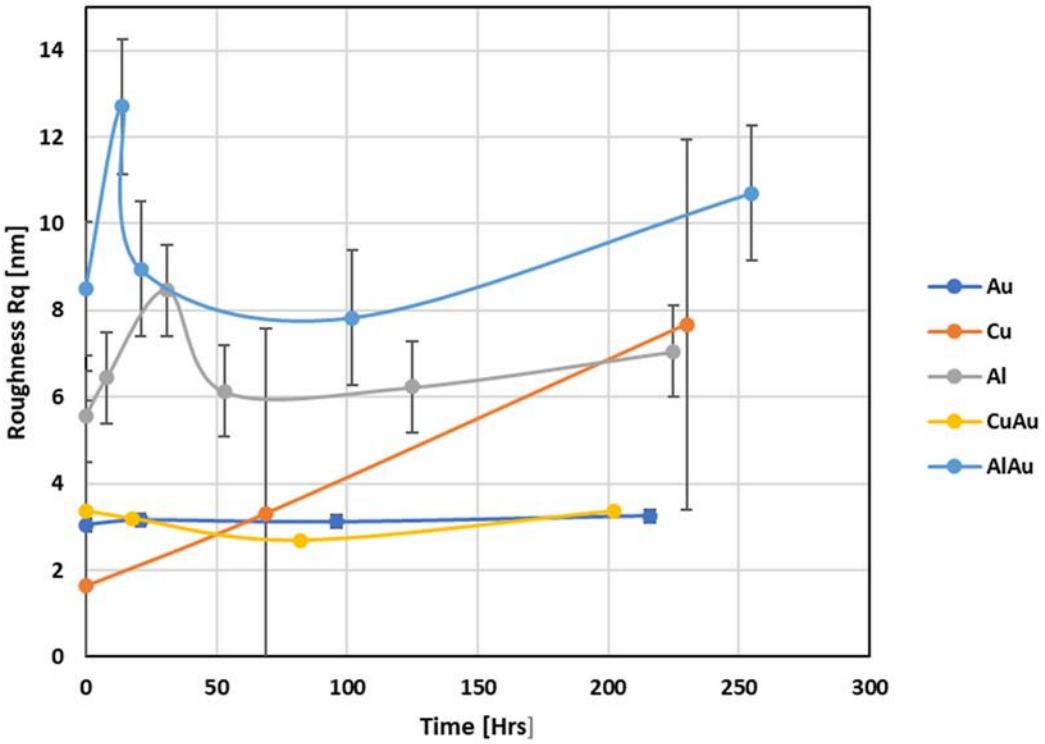

Figure 3-13. Roughness trend for all materials at 65°C

3.2. KPFM CPD

KPFM image contrast can be correlated to surface chemistry changes. As mention in earlier sections, it appears O was present on the surfaces before aging and reacted with the surface which resulted in further oxidation. The surface chemistry is complex. Figure 3-14 shows the 2 μm KPFM image for each sample in the unaged condition (top row) and aged condition (bottom row) in the top group of images and the height sensor images for the same samples and conditions in the bottom group of images.

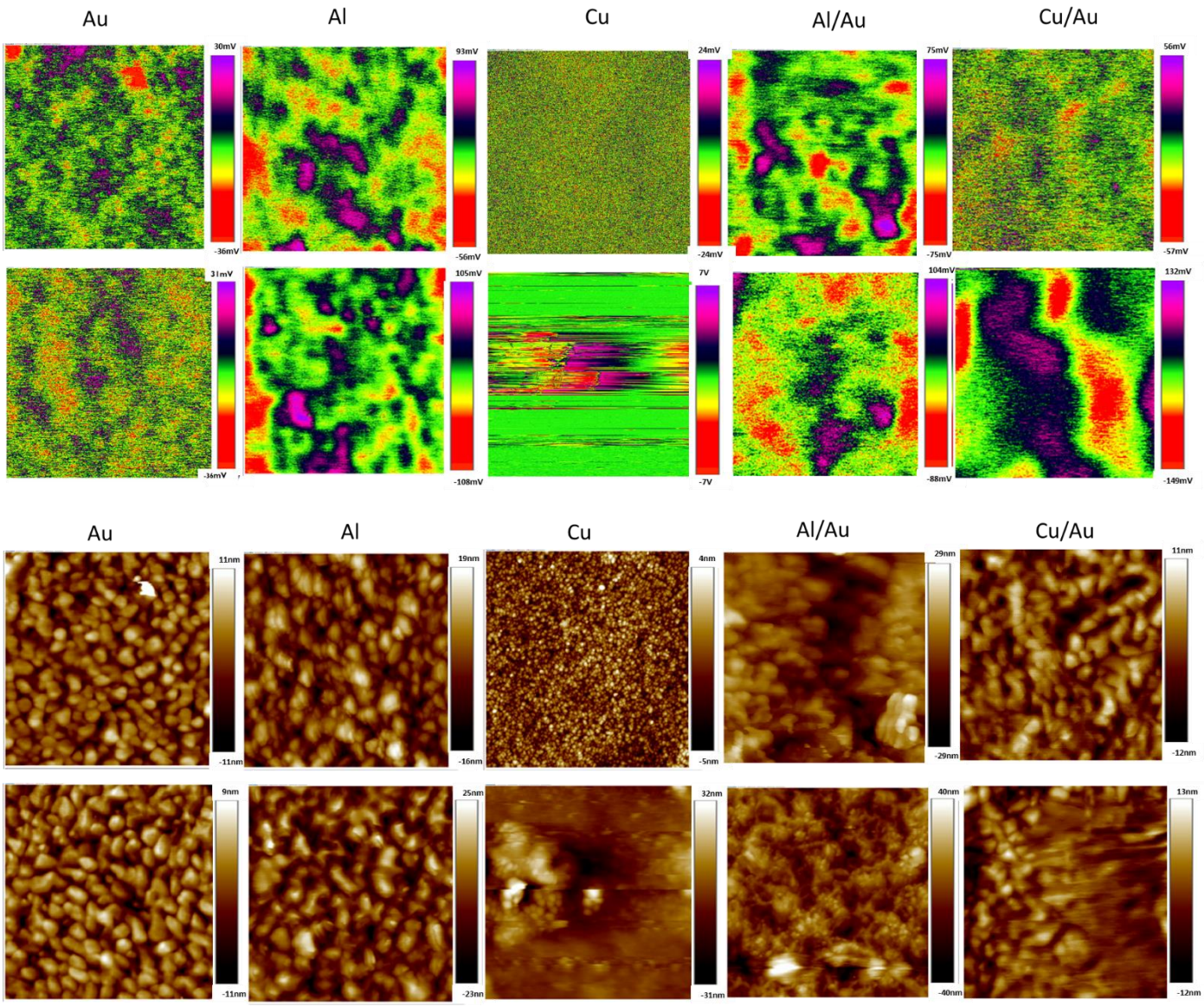

Figure 3-14. Top set of images - 2µm KPFM image for each material – Au, Cu, Al, Al/Au stack and the Cu/Au stack in the unaged condition (top row) and aged condition (bottom row). Bottom set of images – corresponding 2 µm height sensor images. *scaling not normalized

3.2.1. Au Thin Film Standard

Since AES identified C on the Au surface it is reasonable to conclude that contrast in the KPFM image could be due to the surface C identified in the EDS maps. Figure 3-15 shows KPFM images of unaged and aged surface (top) compared with unaged and aged height sensor images (bottom) where the regions showing high CPD values would be Au with less C on the surface. It makes sense that the KPFM contrast will decrease as C concentration increases on the surface as shown in Figure

3-15, b. Figure 3-16 shows the SEM/EDS maps for both the unaged (top) and aged (bottom) Au surface for comparative purposes.

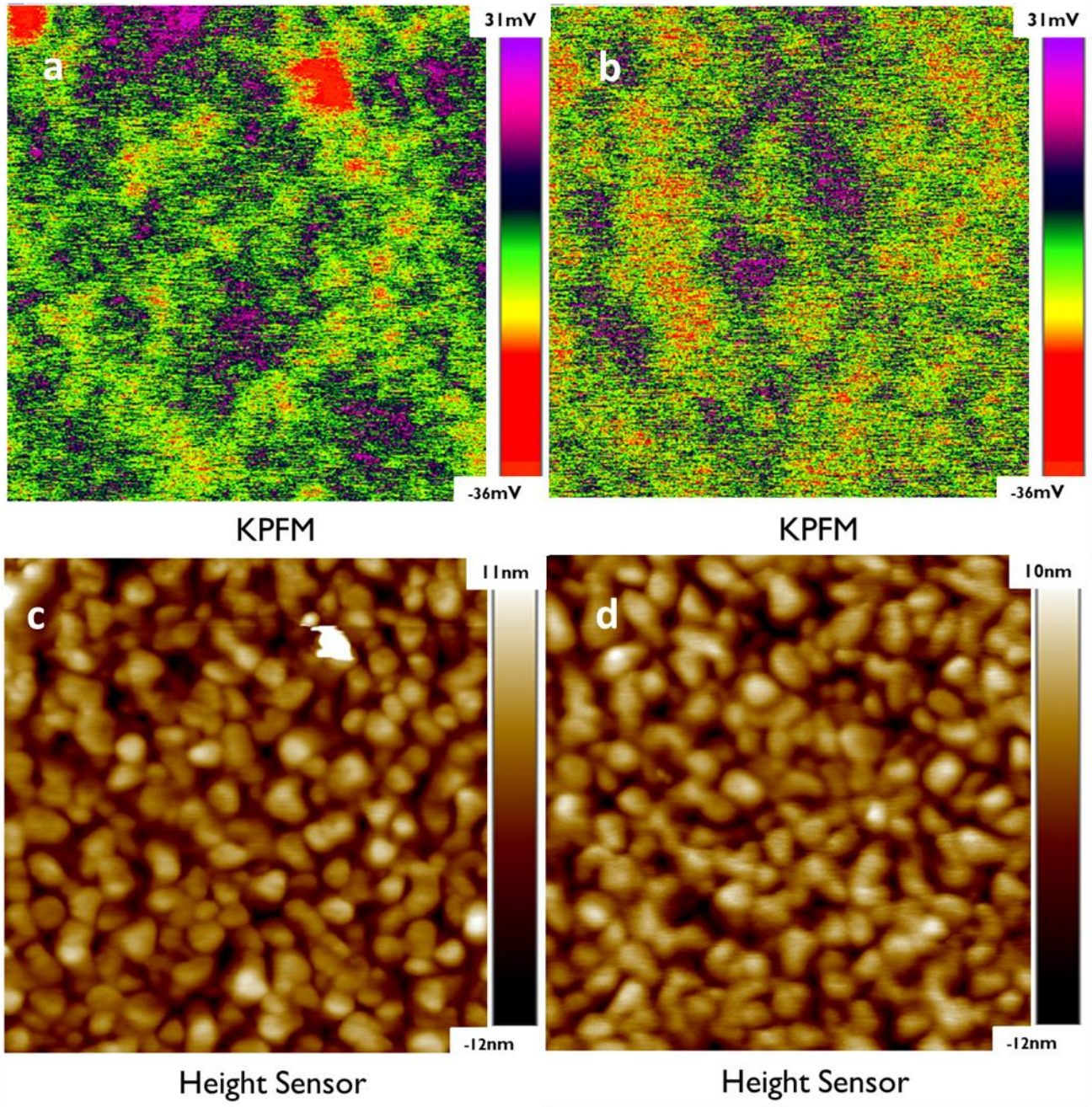

Figure 3-15. 2 µm KPFM images of unaged (a) and aged (b) Au surface compared with 2µm height sensor images of the same surface unaged (c) and aged (d).

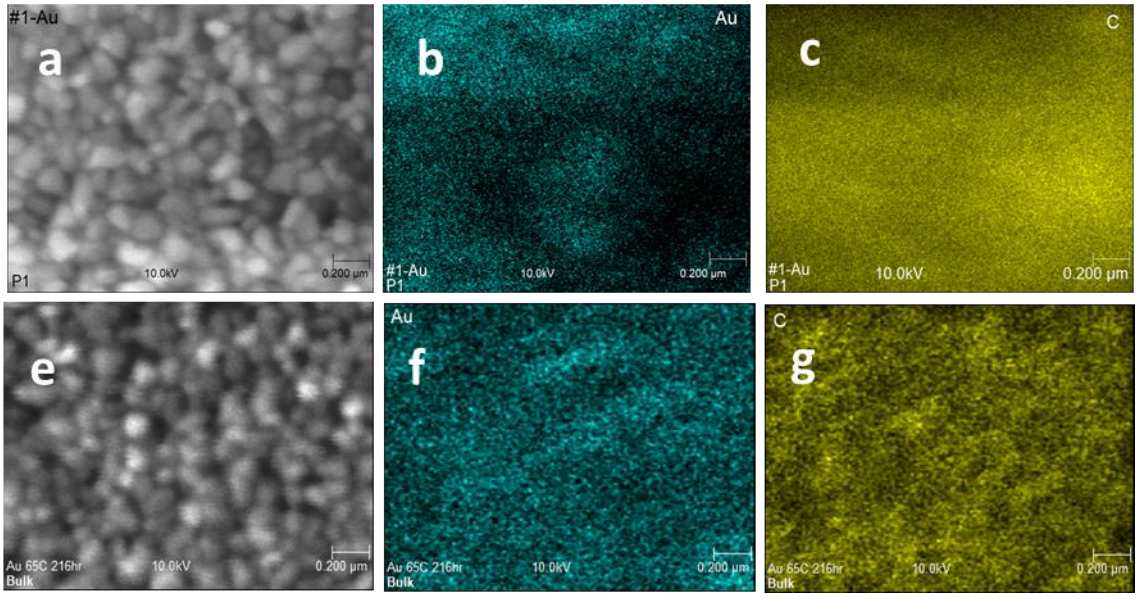

Figure 3-16. 2 µm Auger SEM images (a and e) and elemental maps (b-g) of unaged (top row) and aged (bottom row) of Au surface. C maps (c and g) and Au maps (b and f)

3.2.2. Al Thin Film Standard

Figure 3-17 shows KPFM images of unaged and aged surface (top) compared with unaged and aged height sensor images (bottom) where the regions showing high CPD values would be Al with less C or oxide on the surface. Change in KPFM contrast as surface ages are correlated with increase in C and O concentrations as shown in Figure 3-17, b or possibly the trace contaminants identified in the AES and XPS analysis. Figure 3-18 shows the SEM/EDS maps for both the unaged (top) and aged (bottom) Al surface. AES identified C and O on the Al surface so the contrast in the KPFM image can be correlated to areas with C and O in localized regions covering the Al surface as shown in the EDS maps in Figure 3-18.

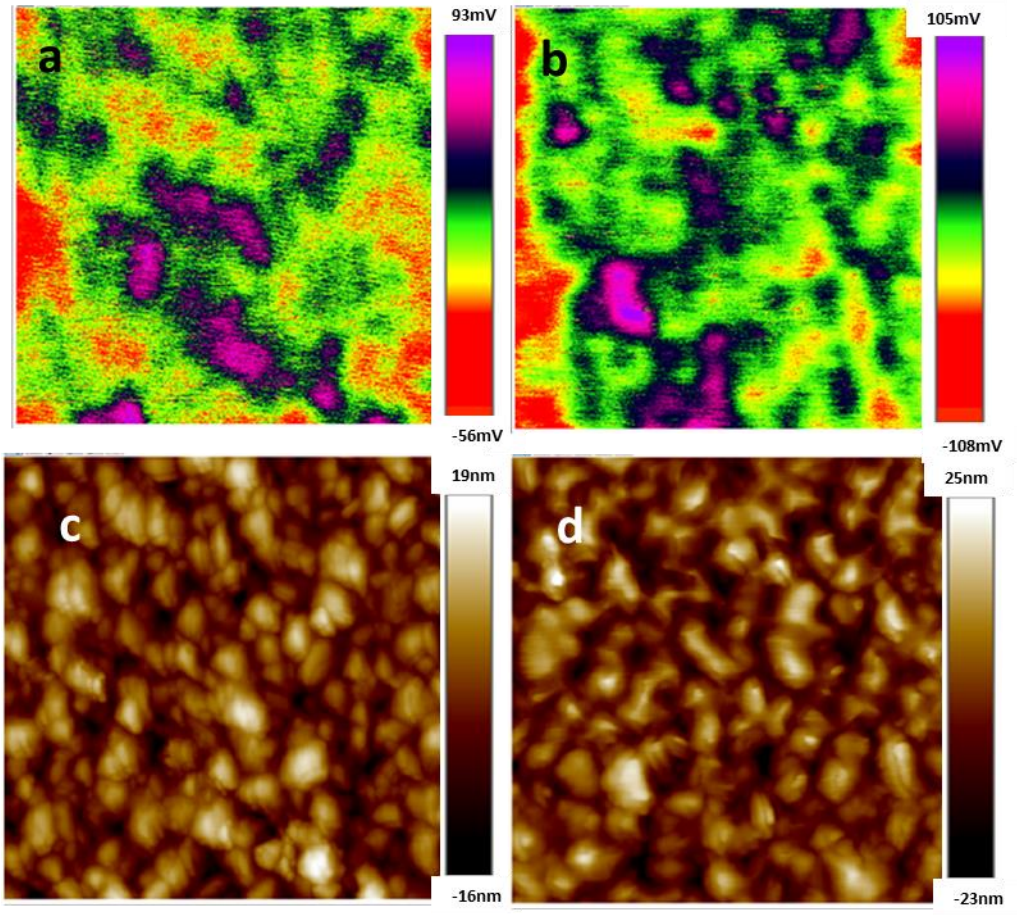

Figure 3-17. 2 µm KPFM images of unaged (a) and aged (b) Al surface compared with 2 µm height sensor images of the same surface unaged (c) and aged (d).

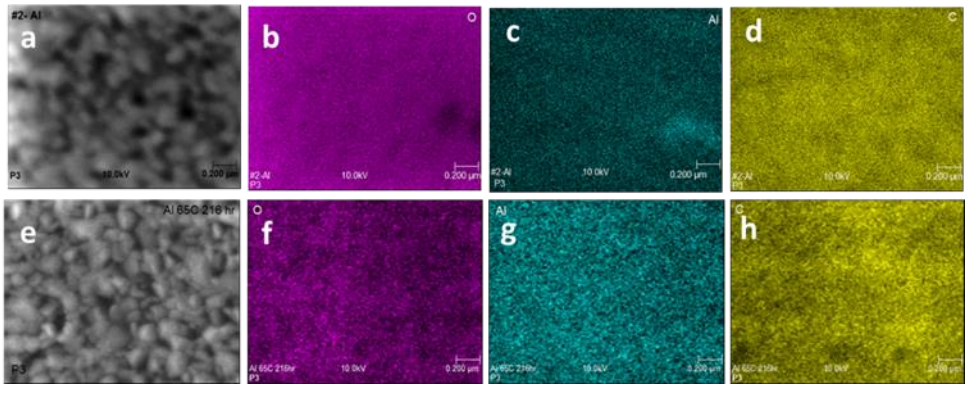

Figure 3-18. 2 µm Auger SEM images (a and e), AES elemental maps (b-g) of unaged (top row) and aged (bottom row) Al surface. O maps (b and f), Al maps (c and g) and C maps (d and h)

3.2.3. *Cu Thin Film Standard*

Particulate formation on the Cu surface made quality imaging impossible as evident in Figure 3-19, b. Figure 3-19 shows KPFM images of unaged and aged surface (top) compared with unaged and aged height sensor images (bottom). No further comments can be made about KPFM images for the Cu standard since acquisition was not possible. Figure 3-20 shows the AES SEM and elemental maps for both the unaged (top) and aged (bottom) Cu surface for comparative purposes.

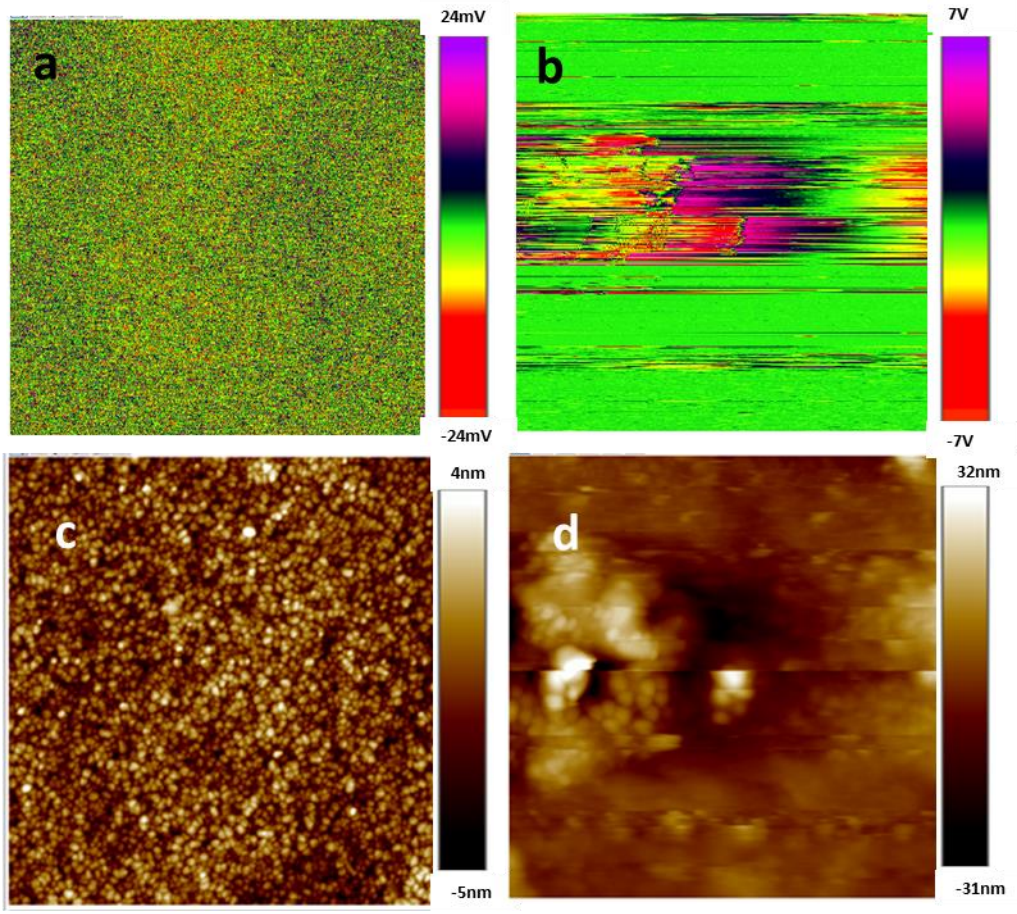

Figure 3-19. 2 µm KPFM images of unaged (a) and aged (b) Cu surface compared with 2 µm height sensor images of the same surface unaged (c) and aged (d).

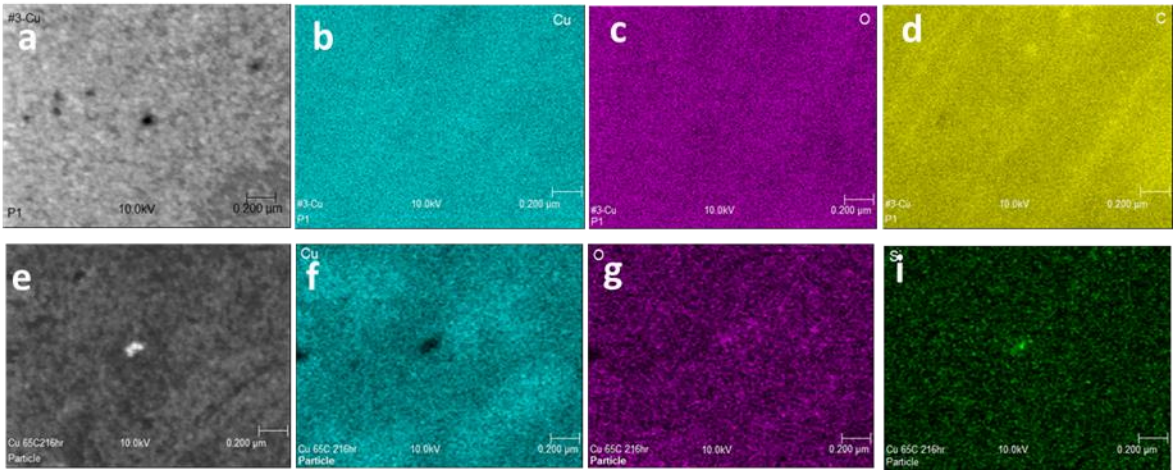

Figure 3-20. 2 µm AES SEM and elemental maps of unaged Cu surface (top) and aged (bottom)

3.2.4. Al/Au Thin Film Stack

Increased contrast in the KPFM image for the Al/Au thin film stack is expected as diffusion is observed, which would indicate compositional differences. However, AES identified Al on the unaged surface which would contribute to the unaged surface KPFM image contrast. Additionally, C and O as well as trace contaminants identified by spectroscopy would also contribute to the KPFM image contrast. KPFM image contrast would change as surface elemental concentration changes over the course of aging as shown in Figure 3-21 where KPFM images of unaged and aged surfaces (top) are compared with unaged and aged height sensor images (bottom). Figure 3-22 shows the SEM and elemental maps for both the unaged (top) and aged (bottom) AlAu surface.

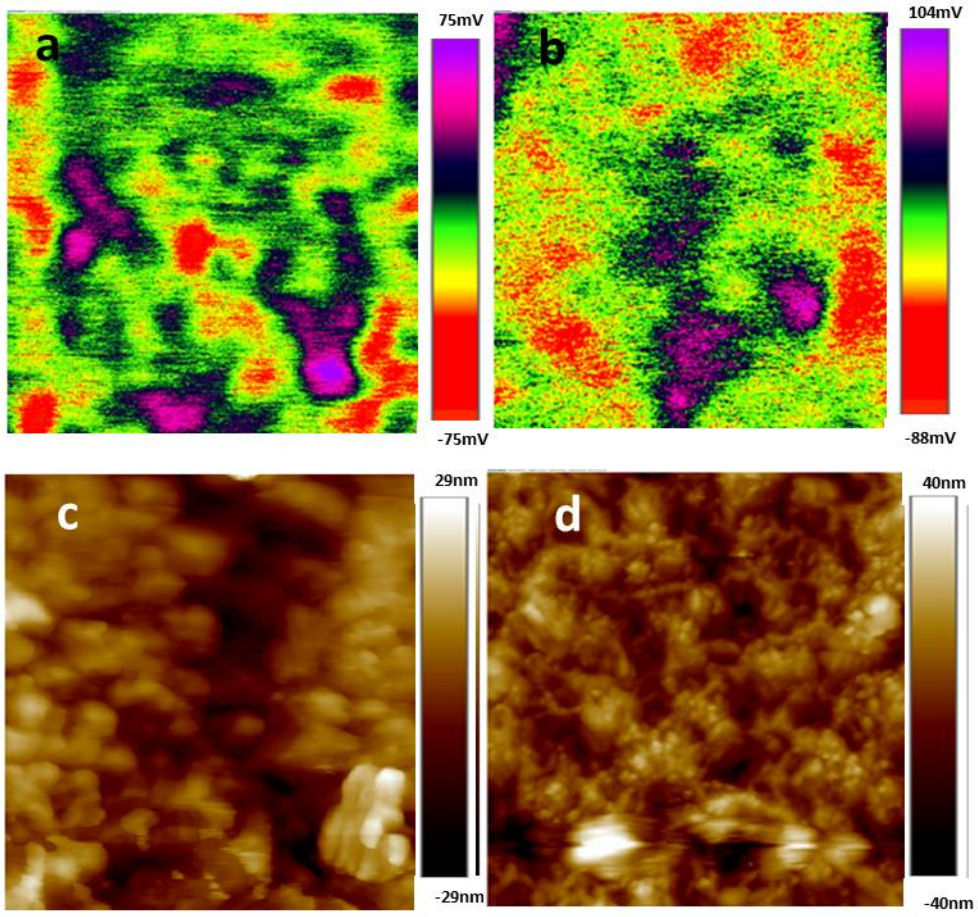

Figure 3-21. 2 µm KPFM images of unaged (a) and aged (b) Al/Au surface compared with 2 µm height sensor images of the same surface unaged (c) and aged (d).

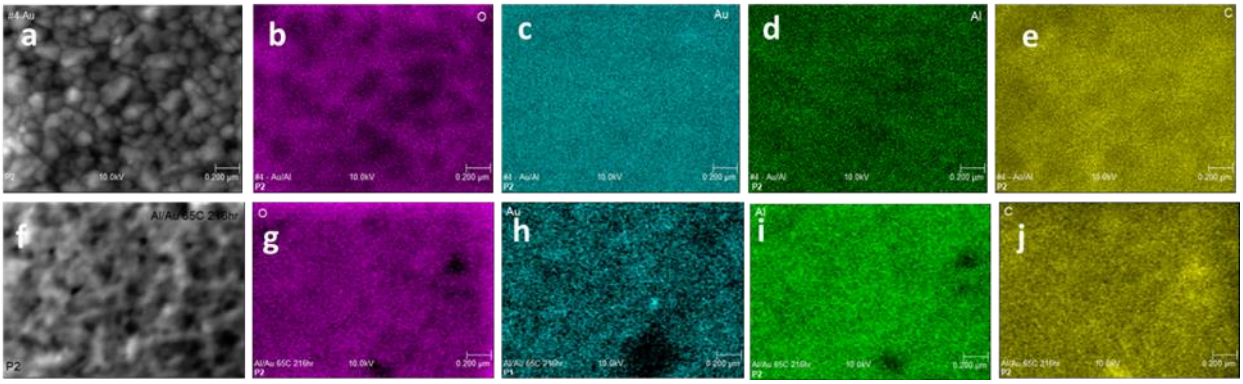

Figure 3-22. AES – 2 µm SEM and elemental maps of Al/Au thin film stack unaged (top) and aged (bottom).

3.2.5. Cu/Au Thin Film Stack

Increased contrast in the KPFM image for the Cu/Au thin film stack is expected as diffusion occurs, which would indicate compositional differences. AES and XPS identified increased concentrations of Cu, C and O as well as the presence of trace contaminants and Au. All these elements would contribute to the KPFM image contrast. Figure 3-23 is KPFM images of unaged and aged surfaces (top), compared with unaged and aged height sensor images (bottom). Figure 3-24 shows the SEM and elemental maps for both the unaged (top) and aged (bottom) AlAu surface.

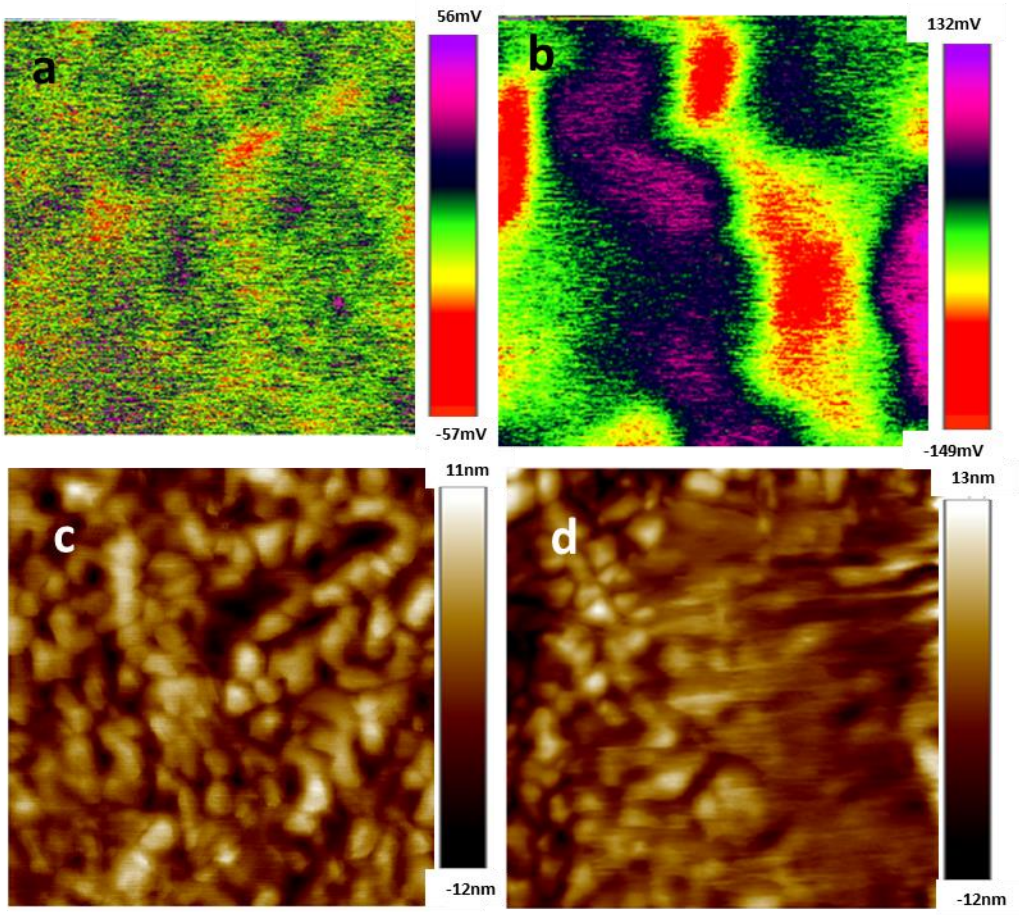

Figure 3-23. 2 µm KPFM images of unaged (a) and aged (b) Cu/Au surface compared with 2 µm height sensor images of the same surface unaged (c) and aged (d).

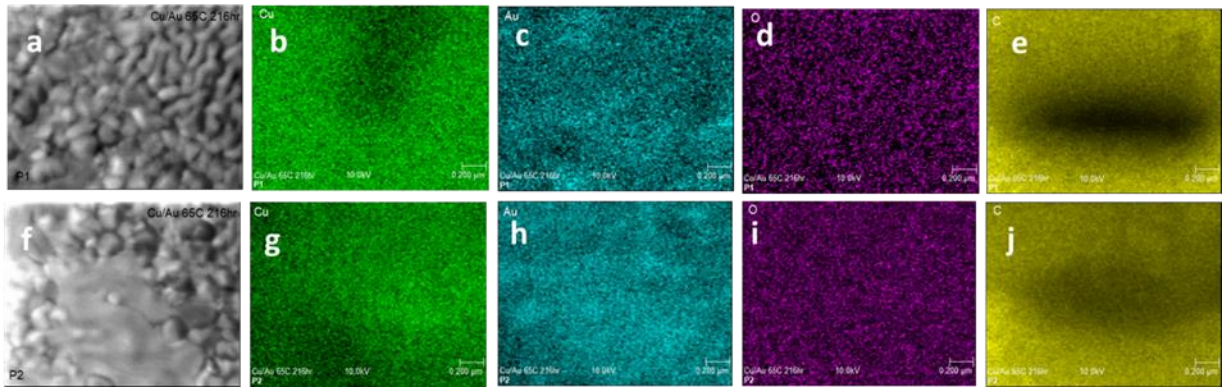

Figure 3-24. AES – 2 µm SEM and elemental maps of Cu/Au thin film of unaged (top) and aged (bottom) surface.

A general decrease in CPD values over the course of the experiment is observed in Figure 3-20. This is likely due to the increase in contamination and oxidation on the surface of these samples. An increase in the Cu thin film standard was observed for the point Vdc measurement which could be due to the conductive nature of CuO_2 oxide versus CUO. The CPD point measurement (Vdc) analysis was done to compare unaged and aged surface CPD values. As previously discussed, the surface chemistry is complex, and the various constituents located at any possible area could have a major impact on the value that was determined by the measurement. Nonetheless standard deviation for surfaces was very small except for the Cu sample that posed a problem for all analysis because of particle formation.

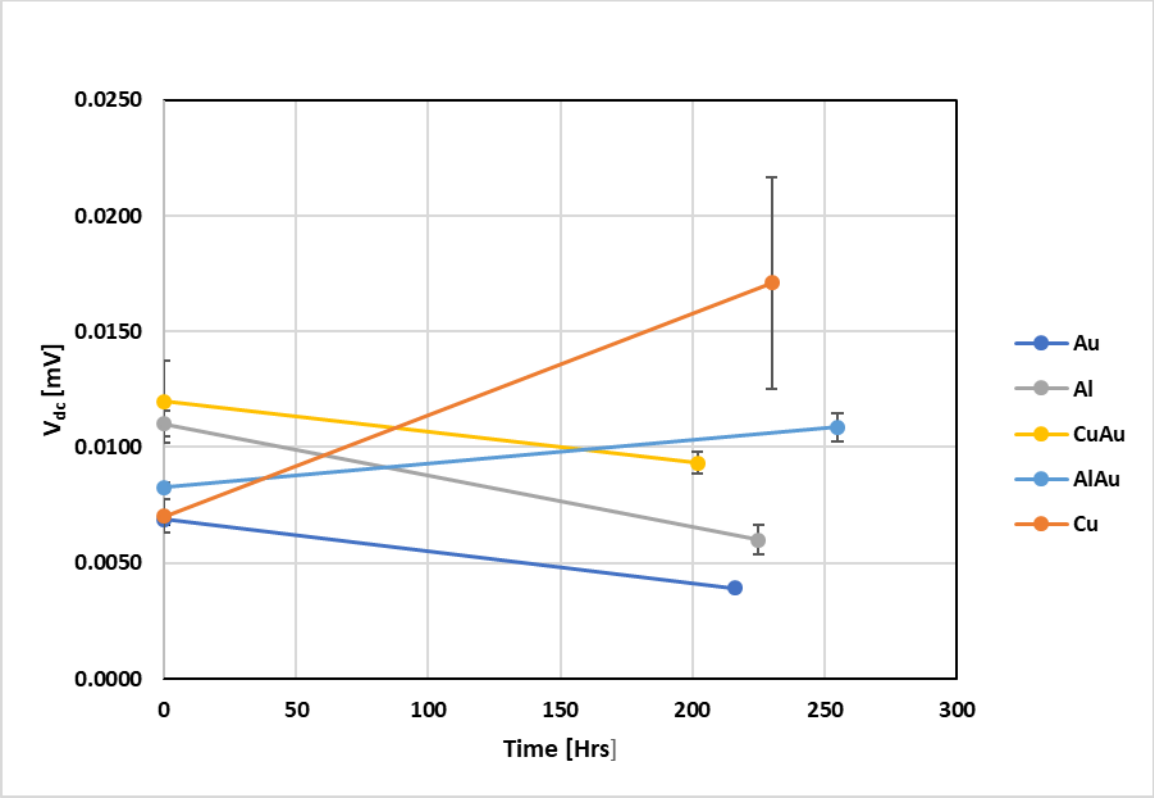

Figure 3-25. Vdc values for unaged and aged samples

3.3. SSRM Resistivity

PF SSRM mode was applied to all surfaces to gather complementary resistivity data to CPD data. An example is shown in Figure 3-26 where the height sensor, DMT modulus, adhesion and log resistance images are shown, respectively. The particle shown yields contrast in all images including a higher resistivity than the surrounding area figure 3-26, d. It is reasonable to conclude that the particle is chemically different that the rest of the surface.

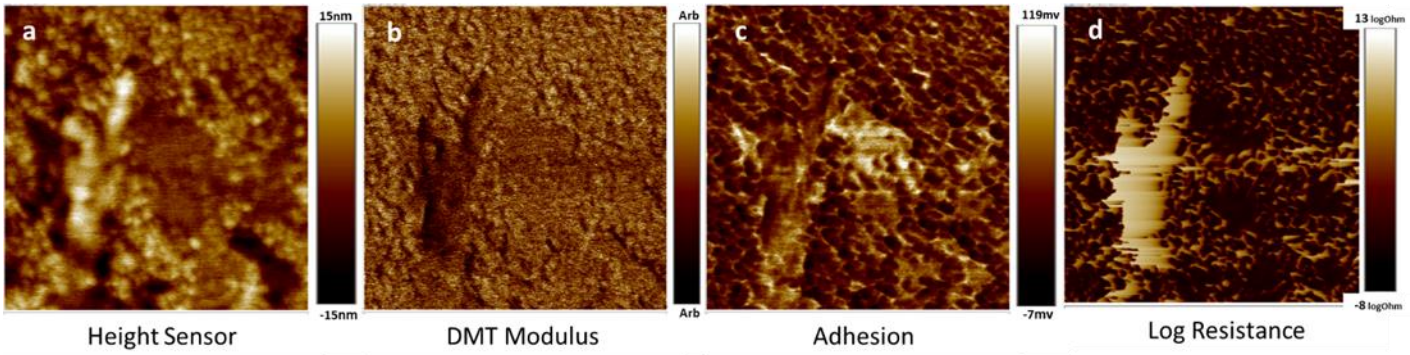

Figure 3-26. 20 µm images of Cu/Au thin film stack. Height sensor (a), DMT modulus (b), adhesion (c) and SSRM

Four areas were analyzed using PF SSRM, averaged and plotted in figure 3-27 which shows an increase in resistivity over the experiment for – Au, Al, Al/Au and Cu/Au surfaces. This is likely due to the increase in oxidation growth on the surface of these samples. A decrease in resistivity for the Cu thin film standard was observed which could be due to the conductive nature of Cu Oxides

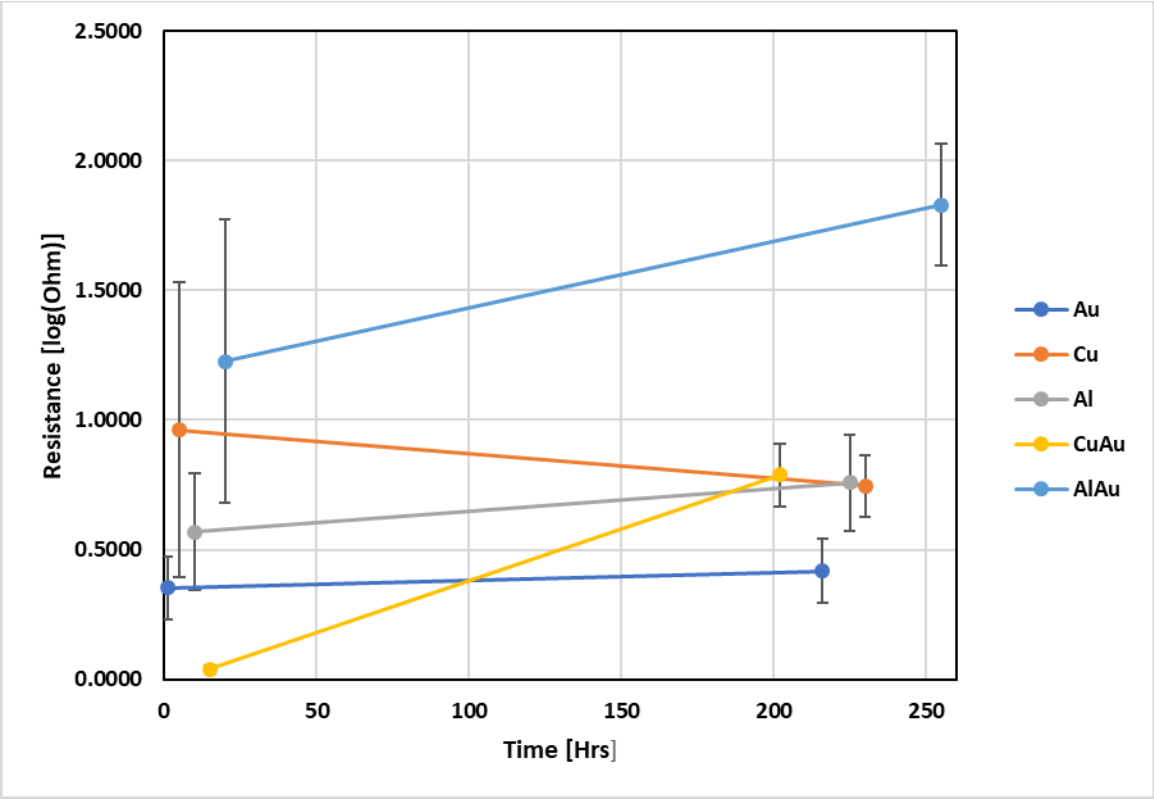

Figure 3-27. An increase in resistivity for – Au, Al, Al/Au and Cu/Au and decrease observed for Cu thin film.

4. DISCUSSION

In this study AFM - KPFM and SSRM modes were developed as an aging characterization technique on thin metal films. over the course of aging at 65°C under dry nitrogen conditions for up to ~200 hours. Surface chemistry has proven to be complex with multiple constituents by AES and XPS and observed via KPFM. Increase in surface C contamination was identified on every surface along with O and trace contaminants. Particulates formed on the Cu surface, Figure 3-6 and 3-7, that began to render imaging increasingly difficult. Vdc point measurements, Figure 3-20, showed a decrease in CPD values over aging for all surfaces except for AlAu thin film stack and Cu likely because of oxidation growth and the electronic nature of the specific oxide. KPFM images showed change in contrast over the course of aging, Figure 3-14. This contrast is caused by the various elements on the surface and their increase in concentration. Elemental maps show underlying metals Al and Cu were present on unaged and aged surfaces Figure 3-10 and 3-12. Concentration of underlying metals on the sample surface did increase over the course of aging, but not in specific regions, which would have indicated preferential grain boundary diffusion. Further studies need to be conducted to understand the nature of diffusion mechanism at play in these thin metal film samples. AES and XPS analysis were performed after full exposure to atmospheric conditions so the surfaces likely oxidized and adsorbed additional abernacious carbon after KPFM analysis which makes comparison between the surfaces somewhat difficult.

The trend in resistivity over the course of aging is not statistically significant, Figure 3-22. The SSRM technique does not have the sensitivity to measure differences in resistivity on unaged and aged surfaces for these aging conditions on these samples.

5. CONCLUSION

The main goal of this work was to develop PF KPFM and PF SSRM as aging characterization techniques. The importance of developing early detection of aging phenomena on the nanoscale has been highlighted in numerous studies [2-4, 8, 12, 15, 22, 30] and focuses on identifying degradation processes before they manifest into latent failures that impact system-level performance and reliability. KPFM and SSRM characterizes nanoscale, surface mechanical and electrical properties as well as surface morphology. The changes in materials related to aging have been identified as morphology changes, oxidation, contamination and diffusion in this study with morphology changes being observed via KPFM as the earliest and most distinct change. The applied techniques are highly sensitive to all surface conditions including effects of oxidation, contamination and humidity. Accordingly, measures were put in place to control environmental conditions and minimize variation associated oxidation and contamination.

Future work could include fabricating and analyzing multi material interplanar matrices. This would allow side-by-side *insitu* analysis of multiple materials, their intermetallics and lend insight into the dominate diffusion mechanism between them. This sort of analysis would eliminate varying environmental conditions including humidity and atmosphere that impact separate analysis. Additionally, continuing this study on a variety of materials, temperatures and time frames would continue to develop the techniques and further explore the capability and limitations of these techniques.

REFERENCES

1. Antler, M., Plated coatings for electrical contacts. in The Role of Coatings in the Prevention of Mechanical Failures. Proc of the 23rd Meeting of the Mechanical Failures Prevention Group. U.S. National Bureau of Standards. Edited by T.R. Shives and W.A. Willard, 1976. 64.
2. F. Echeverría, C.A.B., E. Correa, D. Meza, J. G. Castaño and M. A. Gómez, High Resolution Morphological Changes of Cu, Ni, Al, and Au Surfaces Due to Atmospheric Corrosion. IEEE Transactions on Device and Materials Reliability, June 2017. 17: p. 331-339.
3. Maldonado, R.D.O., A.I. Connection between morphology and electrical resistivity in AuAl films. in 6th International Conference on Electrical Engineering, Computing Science and Automatic Control (CCE). 2009
4. P. Sarobol, S.W., J. Rejent, J. Romero, M. Brumbach, B. McKenzie, and P. Vianco. Understanding Cu-Al Limited-Volume Diffusion Towards Lifetime Prediction for Cu Wire Bonds. in The Rio Grande Symposium on Advanced Materials. 2016. Albuquerque, New Mexico.
5. Holm, R., Electric Contacts. 4 ed. Theory and Application. 1967: New York: Springer-Verlag

6. Greenwood, J.A., Constriction Resistance and the Real Area of Contact. British Journal of Applied Physics 1966. 17: p. 1621.
7. Bowden, F.P., T. David, and G.I. Taylor, The area of contact between stationary and moving surfaces. Proceedings of the Royal Society of London. Series A. Mathematical and Physical Sciences, 1939. 169(938): p. 391-413.
8. Kotula, P.G.a.P., S.V, Visualization of Kirkendall Voids at Cu-Au Interfaces from In Situ TEM Heating Studies. JOM, 2019. 17(10): p. 3521.
9. Karpel, A., Gur, G., Atzmon, Z. et al, Microstructural evolution of gold-aluminum wire-bonds. Journal of Material Science, 2007. 42(7): p. 2347-2357.
10. Pinnel, M.R., Diffusion-related behaviour of gold in thin film systems. Gold Bulletin, 1979. 12(2): p. 62-71.
11. Ballufi, R.W.a.B., J.M, Special Aspects of Diffusion in Thin Films. Thin Solid Films 1975. 25.
12. Berthold, T.B., G; Frammelberger, W; Rodríguez, R; Nafría, M, Nanoscale characterization of copper oxide films by Kelvin Probe Force Microscopy. Thin Solid Films, 2015. 584: p. 310-315.
13. Adamov, M.P., B. and Nenadovic, T., Electrical and structural properties of thin gold films obtained by vacuum evaporation and sputtering. Science direct, 1974. 24(1).
14. Goodman, P., Current and future uses of gold in electronics. Gold Bulletin, 2002. 35(1): p. 21-26.
15. Melo, L.L., Grain Sizes and Surface Roughness in Platinum and Gold Thin Films. Journal of Metastable and Nanocrystalline Materials, 2004. 20: p. 623-628.
16. Holloway, P.H., D.E. Amos, and G.C. Nelson, Analysis of grain-boundary diffusion in thin films: Chromium in gold. Journal of Applied Physics, 1976. 47(9): p. 3769-3775.
17. Duhl, D., K.I. Hirano, and M. Cohen, Diffusion of Iron, Cobalt and Nickel in Gold. Acta Metallurgica, 1963. 11(1): p. 1-&.
18. Pinnel, M.R. and J.E. Bennett, Qualitative observations on the diffusion of copper and gold through a nickel barrier. Metallurgical Transactions A, 1976. 7(5): p. 629-635.
19. Kirkendall, E., The Diffusion of Zinc on Alpha Brass. Trans. AIME, 1942(147): p. 104.
20. Smigelskas, A.K., EO, Zinc Diffusion in Alpha Brass. Trans. AIME, 1947. 171: p. 130.
21. Lee, H., et al., Surface Potential Analysis of Nanoscale Biomaterials and Devices Using Kelvin Probe Force Microscopy. J. Nanomater., 2016. 2016: p. 4209130.

22. Kaja, K., Development of Nano-probe Techniques for Work Function Assessment and Application to Materials for Microelectronics, in School of Physics. 2010, University of Grenoble: Grenoble.
23. Cohen, G., et al., Reconstruction of Surface Potential from Kelvin Probe Force Microscopy Images. Nanotechnology, 2013. 24: p. 295702.
24. Glatzel, T., et al., Determination of Effective Tip Geometries in Kelvin Probe Force Microscopy on Thin Insulating Films. Nanotechnology, 2009. 20: p. 164016.
25. Hua, U., Advanced AFM Applications Training Class - KPFM. 2016, Bruker.
26. Melitz, W., et al., Kelvin Probe Force Microscopy and its Application. Surf. Sci. Rep., 2011. 66: p. 1-27.
27. Nony, L., et al., On the Relevance of the Atomic-Scale Contact Potential Difference by Amplitude-Modulation and Frequency-Modulation Kelvin Probe Force Microscopy. Nanotechnology, 2009. 20: p. 264014.
28. O'Boyle, M.P., T.T. Hwang, and H.K. Wickramasinghe, Atomic Force Microscopy of Work Functions on the Nanometer Scale. Appl. Phys. Lett., 1999. 74(18): p. 2641-2642.
29. Polak, L. and R.J. Wijngaarden, Preventing Probe Induced Topography Correlated Artifacts in Kelvin Probe Force Microscopy. Ultramicroscopy, 2016. 171: p. 158-165.
30. Enevoldsen, G.H., et al., Atomic Scale Kelvin Probe Force Microscopy Studies of the Surface Potential Variations on the TiO2 (110) Surface. Phys. Rev. Lett., 2008. 100: p. 236104.
31. Kou, L., et al., Surface Potential Imaging with Atomic Resolution by Frequency-Modulation Kelvin Probe Force Microscopy Without Bias Voltage Feedback. Nanotechnology, 2015. 26: p. 195701.
32. Scanning Probe Microscopy. Electrical and Electromechanical Phenomena at the Nanoscale. Vol. 1. 2007: Springer.
33. Baca, A.B., M.; Vianco, P.; Scrymgeour, D.; Patterson, B., Grain Boundary Diffusion Characterized by KPFM. 2018, Sandia National Labs.
34. Nanoscope software Available from: https://www.bruker.com/products/surface-and-dimensional-analysis/atomic-force-microscopes/dimension-icon/overview.html.
35. Adeva, P., et al., Microstructure and High Temperature Mechanical Properties of Tin. Mater. Sci. Eng., A, 1995. 194: p. 17-23.
36. Antler, M., IEEE Transactions on Parts, Hybrids and Packaging 1973. 9.
37. Jiang, C.-S., et al., Local Built-In Potential on Grain Boundary of Cu(In,Ga)Se2 Thin Films. Appl. Phys. Lett., 2004. 84(18): p. 3477-3479.
38. Lü, J., et al., Kelvin Probe Force Microscopy on Surfaces: Investigation of the Surface Potential of Self-Assembled Monolayers on Gold. Langmuir, 1999. 15(23): p. 8184-8188.
39. Michaelson, H.B., The Work Function of the Elements and its Periodicity. J. Appl. Phys., 1977. 48(11): p. 4729-4733.
40. Nazarchuk, Y.N., V.A. Novikov, and N.A. Torkhov, Investigation Into the Effect of Size of Local Metallization of N-GaAs Surface on the Character of Surface Potential Distribution Determined by Atomic-Force Microscopy. Russ. Phys. J., 2011. 54(3): p. 296-300.
41. Nonnenmacher, M., M.P. O'Boyle, and H.K. Wickramasinghe, Kelvin Probe Force Microscopy. Appl. Phys. Lett., 1991. 58(25): p. 2921-2923.
42. Ouyang, J., et al., Programmable Polymer Thin Film and Non-Volatile Memory Device. Nat. Mater., 2004. 3: p. 918-922.
43. Panchal, V., et al., Standardization of Surface Potential Measurements of Graphene Domains.
44. Revilla, R.I., et al., Local Corrosion Behavior of Additive Manufactured AlSiMg Alloy Assessed by SEM and SKPFM. J. Electrochem. Soc., 2017. 164(2): p. C27-C35.

45. Riviére, J.C., The Work Function of Gold. Appl. Phys. Lett., 1966. 8(7): p. 172.
46. Sadewasser, S., et al., Influence of Uncompensated Electrostatic Force on Height Measurements in Non-Contact Atomic Force Microscopy. Nanotechnology, 2004. 15: p. S14-S18.
47. Schmutz, P. and G.S. Frankel, Characterization of AA2024-T3 by Scanning Kelvin Probe Force Microscopy. J. Electrochem. Soc., 1998. 145(7): p. 2285-2295.
48. Shoucair, F.S., Potential and problems of high-temperature electronics and CMOS integrated circuits (25–250°C) - an overview. Elsevier, 1991. 22(2): p. 39-54.
49. Tompkins, H.G. and M.R. Pinnel, Low-temperature diffusion of copper through gold. Journal of Applied Physics, 1976. 47(9): p. 3804-3812.
50. Yin, J., C. D'Haesem, and B. Nystenm, Surface Electrical Properties of Stainless Steel Fibers: an AFM-Based Study. Appl. Surf. Sci., 2015. 330: p. 67-73.
51. Zhao, M., et al., Ultrasharp and High Aspect Ratio Carbon Nanotube Atomic Force Microscopy Probes for Enhanced Surface Potential Imaging. Nanotechnology, 2008. 19: p. 235704.

DISTRIBUTION

Email—Internal

Name	Org.	Sandia Email Address
Ana Baca	01819	abtruji@sandia.gov

This page left blank

This page left blank

Sandia National Laboratories

Sandia National Laboratories is a multimission laboratory managed and operated by National Technology & Engineering Solutions of Sandia LLC, a wholly owned subsidiary of Honeywell International Inc. for the U.S. Department of Energy's National Nuclear Security Administration under contract DE-NA0003525.